Chapter 10

TEST RESULTS AND ANALYSIS

10.1 Introduction

In this chapter, the interpretation and analysis of data acquired using the acquisition system are presented. The data acquisition system was programmed to generate data in certain specified time intervals, usually at ten seconds initially for a short period of time at the start of a test and then at intervals of five minutes. Each acquisition consisted of ten seconds of data written in a text file, which included all strain gauge and thermocouple data. Data from each strain gauge acquired at each ten seconds interval were analyzed to calculate resilient and permanent strain. The compilation of all acquisitions throughout the test generated the resilient and permanent strain histories for each strain gauge. The resilient and permanent strain histories were then analyzed to determine failure strain and corresponding load level. Determination of failure load and several other analytical studies based on acquired data are presented in the following sections.

10.2 Strain Time Histories

Movement of wheel on top of the HMA slabs generated stress pulses in the pavement, which in turn created strain pulses. A typical strain output for one cycle of loading is shown in **Figure 10.1(a)** (for transverse strain gauge) and **Figure 10.1(b)** (for longitudinal strain gauge).

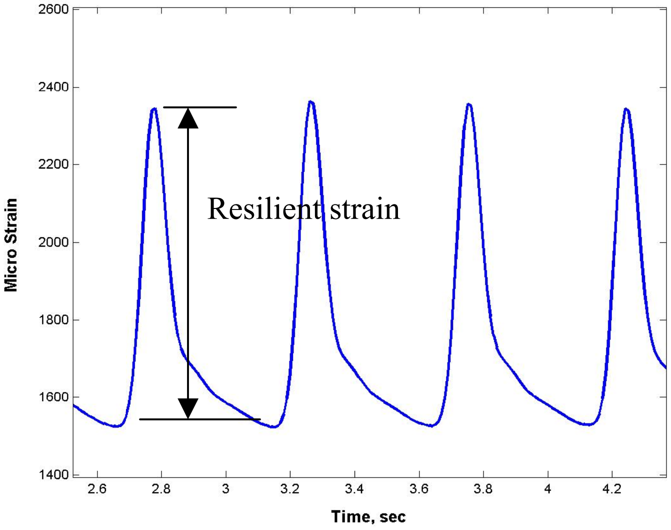

(a)

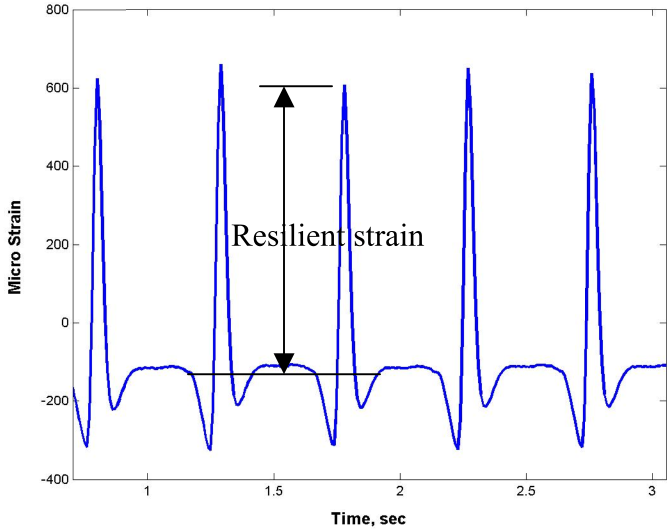

(b)

Figure 10.1: (a) Transverse strain history, (b) Longitudinal strain history

As can be seen form **Figure 10.1**, the two time histories are different. The transverse strain gauge recorded tensile strains only and longitudinal strain gauges recorded strains both in tension and compression. This is in agreement with results presented in [**16,17**]. The resilient strain was calculated as maximum recoverable strain in 10 seconds of data acquisition for both longitudinal and transverse strain gauges. The permanent strain was calculated as the difference between average strains of two successive acquisitions.

10.2.1 Resilient and Permanent Strain History

Once resilient and average strain for each acquisition was calculated, these strains were plotted against time for whole duration of test. The permanent and resilient strains of Slab J, K, L and N are shown in **Figure 10.2(a), (b), (c), (d), (e), (f), (g), (h)**.

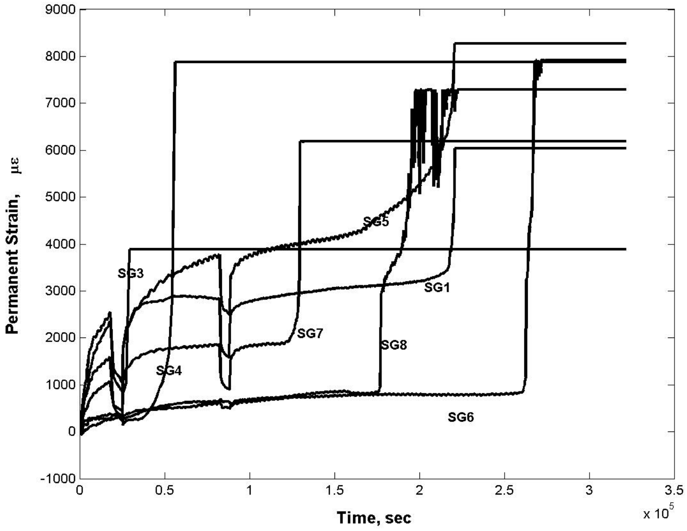

Figure 10.2 (a): Permanent strain history for Slab J. SG4,6,8= longitudinal

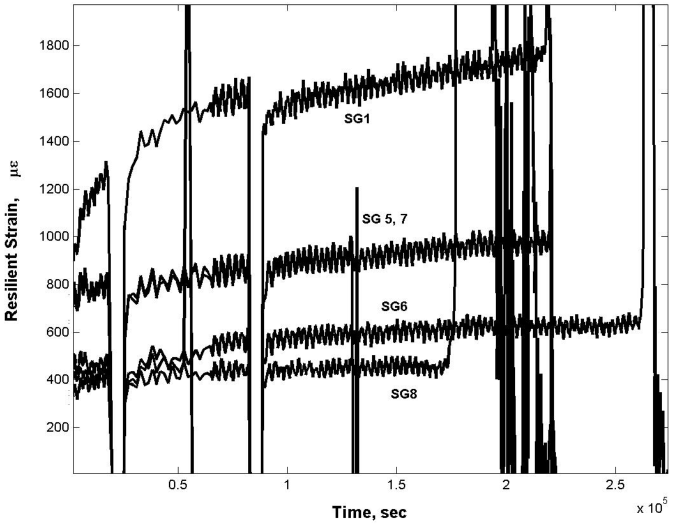

Figure 10.2 (b): Resilient strain history for Slab J. SG4,6,8= longitudinal

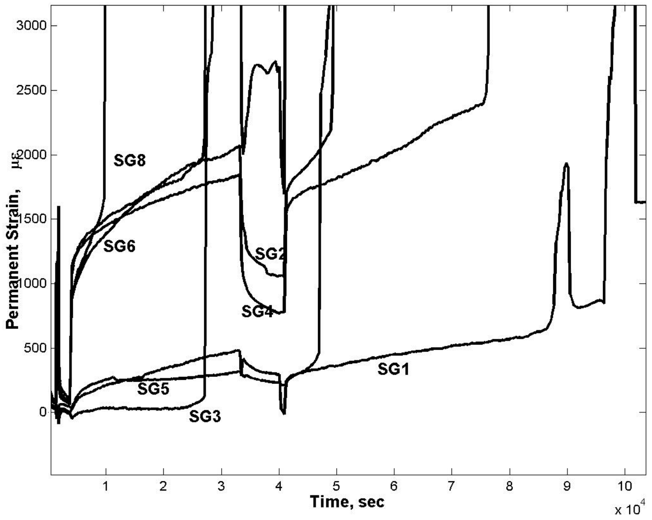

Figure 10.2 (c): Permanent strain history for Slab K. SG1,3,5= longitudinal

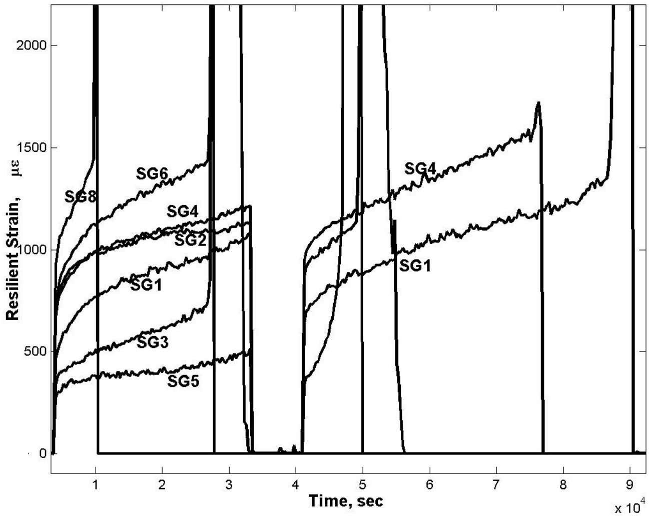

Figure 10.2 (d): Resilient strain history for Slab K. SG1,3,5= longitudinal

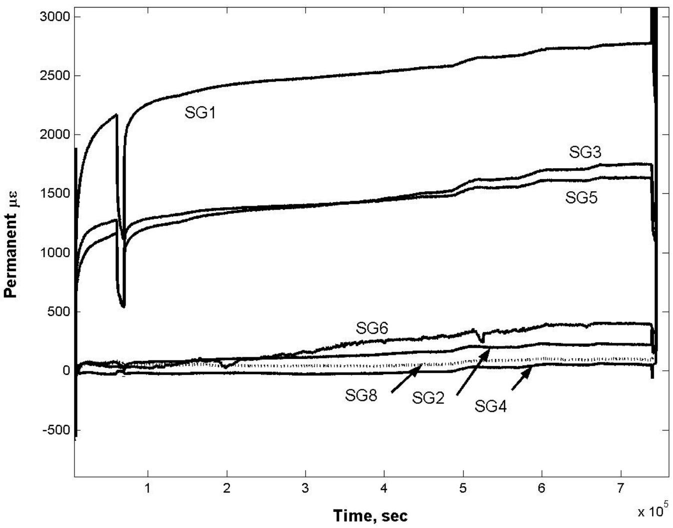

Figure 10.2 (e): Permanent strain history for Slab L. SG2,4,6,8= longitudinal

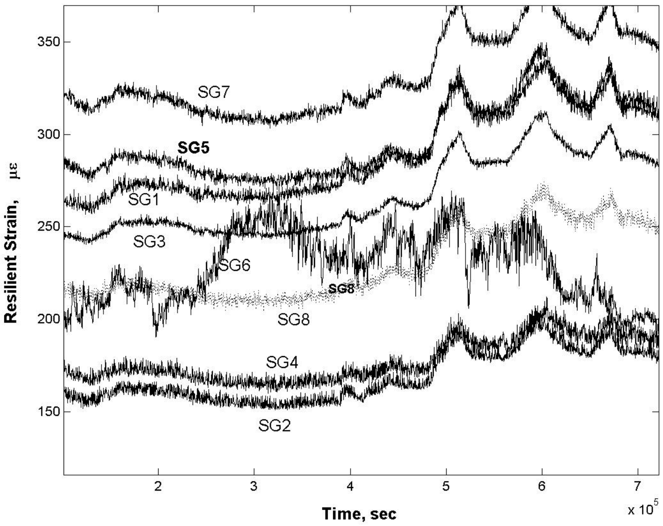

Figure 10.2 (f): Resilient strain history for Slab L. SG2,4,6,8= longitudinal

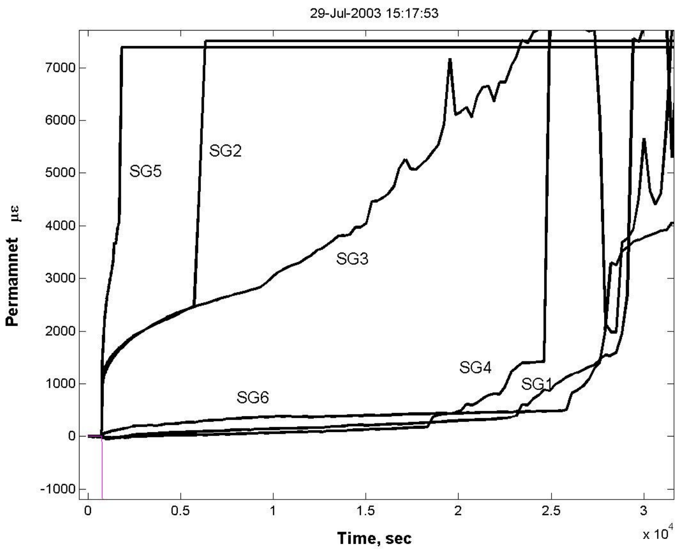

Figure 10.2 (g): Permanent strain history for Slab N. SG1,4,6=longitudinal

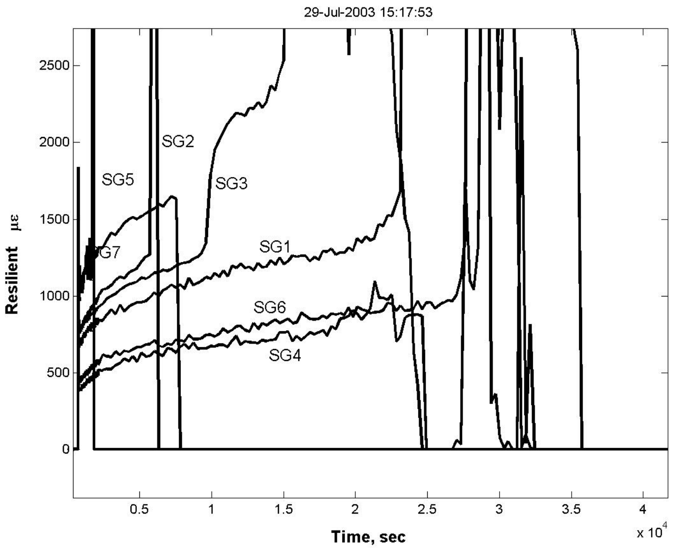

Figure 10.2 (h): Resilient strain history for Slab N. SG1,4,6=longitudinal

The plots in **Figure 10.2** also show the strain history when no load is acting (the machine is at rest). Several points can be noted from the plots:

1. It is clear from the plots that the transverse strain gauges show much higher resilient and permanent viscoelastic strains compared to longitudinal strain gauges. Transverse strain gauges are entirely in tension and longitudinal strain gauges are in both tension and compression. Moreover, the rate of increase in

permanent strain is higher in the transverse strain gauge than in the longitudinal strain gauges. These findings are similar to observations made by Rowe and Brown [**17**].

2. In some of the plots, it is evident that there was a contact problem with the wire, where the strain suddenly reached higher values and then returned to lower values and then reached higher again and hence did not show a monotonic increase of strain. In subsequent analysis, only data from the strain gauges showing consistent results throughout the experiment were selected.

3. Plots of permanent and resilient strains show a basic pattern of strain variation when load is acting, that is, each strain history has three distinctive phases:
    a. the primary phase of decreasing rate of strain increase
    b. the secondary phase of constant rate of strain increase and
    c. the tertiary phase of increasing rate of strain increase.

   This is shown schematically in **Figure 10.3**, where ε_f represents failure strain and t_f represents failure time (corresponding to failure load N_f).

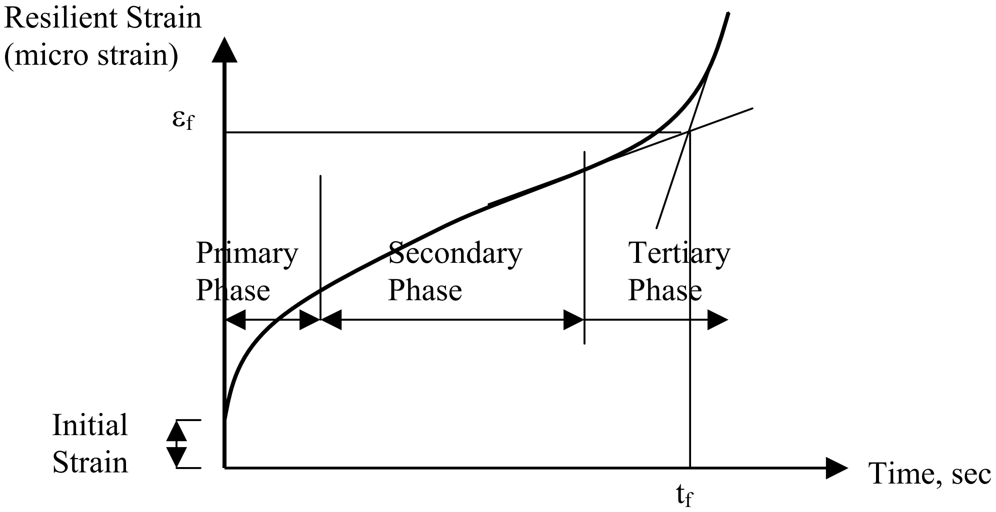

Figure 10.3: Schematic diagram of typical resilient strain history

This pattern is evident throughout the time history as well as between two stoppage times. Although this behavior is exhibited by both transverse and longitudinal strain gauges, the secondary phase is more prominent over the primary phase for longitudinal strain gauges compared to transverse strain gauges.

4. Stopping the machine resulted in typical relaxation curves with almost the same rate of relaxation (between stopping and subsequent starting time) indicating similar relaxation behavior for any part of slab.

5. Data corresponding to start of machine after a stoppage showed quick build up of permanent and resilient strain.

10.3 Temperature Time Histories

The target temperature for each test was 20^{o}C. However, due to long test duration and relatively higher ambient temperature, the temperature during the tests varied over a range. The temperature time histories are shown in **Figure 10.4(a), (b), (c), (d)**.

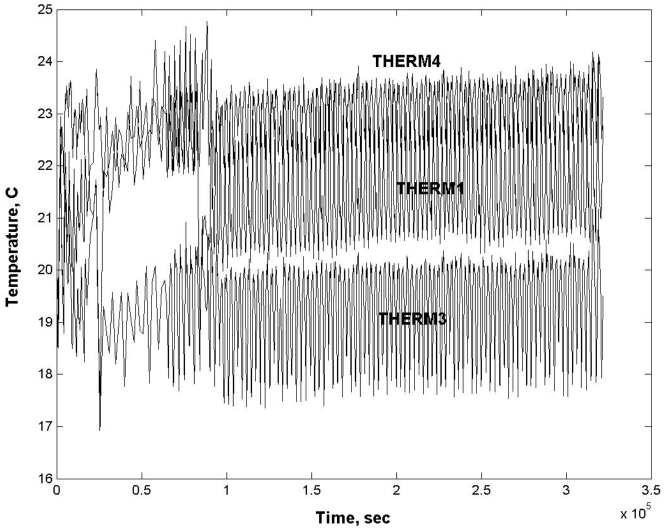

Figure 10.4 (a): Variation of temperature for Slab J

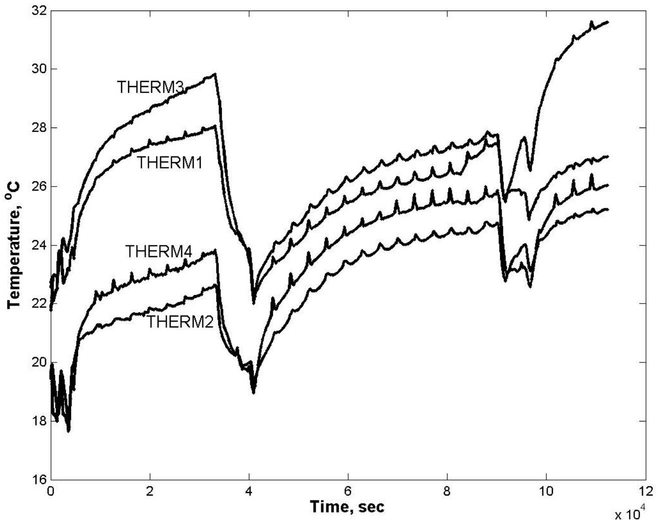

Figure 10.4 (b): Variation of temperature for Slab K

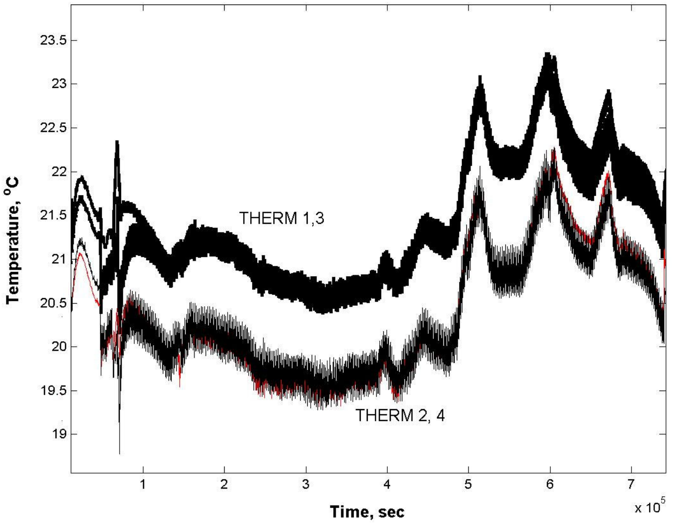

Figure 10.4 (c): Variation of temperature for Slab L

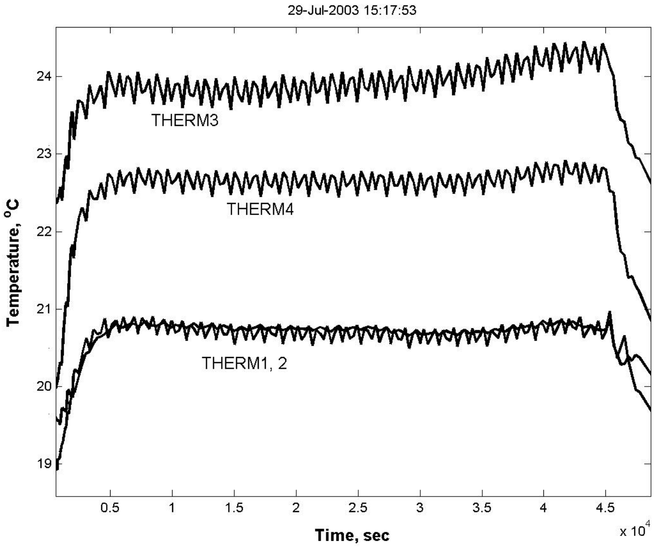

Figure 10.4 (d): Variation of temperature for Slab N

In **Figure 10.4** the plots of temperature variation show extremely uniform variation over the entire duration of test (97 hours for Slab J and 12 hours for N). For the other two slabs, temperature plots in **Figure 10.4(b)** and **10.4(c)** show some variations over entire duration of test. Keeping in mind that it was very difficult to maintain exact target temperature for entire duration of the test for the reasons stated above, the plots show the variations were within two degrees Celsius for Slab L and within five degrees Celsius for Slab K. In the following discussion, strain data used are those data obtained directly by acquisition; later a procedure for compensating the effect of temperature variation on strain is discussed.

10.4 Strain and Load at Failure

The nature of material as indicated in primary and secondary phase of loading is changed at the onset of tertiary phase when the rate of increase of strain with load application started to increase significantly (**Figure 10.3**). Therefore, the strain and load corresponding to the onset of tertiary phase can be regarded as the failure strain and load respectively. Initial strain for each strain gauge was calculated from acquisition data when the stable response was obtained at the initial portion of the data. The failure strain and load for each strain gauge were calculated from the point of intersection of straight lines in secondary phase and tertiary phase as shown in **Figure 10.3**. While calculating this strain, the strain gauges showing consistent results were selected. Initial strains and failure loads were thus obtained for both transverse and longitudinal direction for each test slab. **Table 10.1** shows all strain data corresponding to failure. This data has been analyzed and inferences have been drawn in the following sections.

Table 10.1: Initial strains, failure load and test temperatures for test slabs

Slab ID	**Strain Gauge Number**	**Direction of SG**	**Initial Strain, μm/m**	**Failure Load, N_f**	**Average Temp, ^{o}C**
J	1	Tr	734	406712	T1 = 21.5
	3	Tr	323		T2 = 19.8
	5	Tr	625	416914	T3 = 19.4
	7	Tr	616	233284	T4 = 22.7
	2	Lng			Avg = 20.9
	4	Lng	310		
	6	Lng	341	497928	
	8	Lng	263	317298	
K	2	Tr	653		25.6
	4	Tr	664	124860	21.7
	6	Tr	678	27860	25.4
	8	Tr	897		22.1
	1	Lng	452	134860	Avg = 23.7
	3	Lng	323	26860	
	5	Lng	250		
	7	Lng			
L	1	Tr	202	9800000	21.3
	3	Tr	189	9800000	20.3
	5	Tr	221	9800000	21.5
	7	Tr	253	9800000	20.2
	2	Lng	125	9800000	Avg = 20.8
	4	Lng	144	9800000	
	6	Lng	170	9800000	
	8	Lng	166	9800000	

Table 10.1: Initial strains, failure load and test temperatures for test slabs (Cont.)

Slab ID	Strain Gauge Number	Direction of SG	Initial Strain, μm/m	Failure Load, N_f	Average Temp, ^oC
N	2	Tr	720		19.9
	3	Tr	769	14740	20.1
	5	Tr	922		23.3
	7	Tr	1014		21.5
	1	Lng	640	34494	Avg = 21.2
	4	Lng	366	29742	
	6	Lng	403	50746	
	8	Lng			
P	2	Tr	1031	99830	24.9
	4	Tr			24.6
	6	Tr			26.9
	8	Tr			25.9
	1	Lng	768		Avg = 25.6
	3	Lng	407	107030	
	5	Lng	565	42950	
	7	Lng	407	112790	
Q	1	Tr	779	38106	24.8
	3	Tr	691		21.8
	5	Tr	590	36306	NA
	7	Tr	630	39906	25.1
	2	Lng	277	122162	Avg = 23.9
	4	Lng	548	21906	
	6	Lng	290	51906	
	8	Lng	368		
R	2	Tr	357	429054	
	4	Tr	333	648790	
	6	Tr	396		
	8	Tr	449		
	1	Lng	276	496260	Avg = 19.3
	3	Lng	160	618676	
	5	Lng	164	443406	
	7	Lng	214	678790	

Table 10.1: Initial strains, failure load and test temperatures for test slabs (Cont.)

Slab ID	Strain Gauge Number	Direction of SG	Initial Strain, μm/m	Failure Load, N_f	Average Temp, °C
S	2	Tr	328		
	4	Tr	379		
	6	Tr	380		
	8	Tr			
	1	Lng	171		Avg = 17.4
	3	Lng	216	858224	
	5	Lng	170		
	7	Lng	199		
T	2	Tr	251	190616	
	4	Tr	288	290234	
	6	Tr	300	378450	
	8	Tr			
	1	Lng	151	1069914	Avg = 15.0
	3	Lng	131		
	5	Lng	149	902488	
	7	Lng	178	647892	

Blank Cell = data not available due to improper function and/or breakage of strain gauges

The average initial strain and corresponding failure load for both directions were obtained for each test slab, thus giving a pair of data set for each test slab as indicated in **Table 10.2**. The results have been discussed in the following sections.

Table 10.2: Average strains for test slabs

Slab ID	Average Initial Strain	Average Failure Load	Direction
J	575	352303	Transverse
	305	407613	Longitudinal
K	723	76360	Transverse
	342	80860	Longitudinal

Table 10.2: Average strains for test slabs (Cont.)

Slab ID	Average Initial Strain	Average Failure Load	Direction
L	216	Did not fail	Transverse
	151	Did not fail	Longitudinal
N	856	14740	Transverse
	470	38327	Longitudinal
P	1031	99830	Transverse
	537	87590	Longitudinal
Q	673	38106	Transverse
	371	65325	Longitudinal
R	384	538922	Transverse
	204	559283	Longitudinal
S	362		Transverse
	189	858224	Longitudinal
T	280	286433	Transverse
	152	873431	Longitudinal

10.5 Stiffness Corresponding to Failure Load

The damage to the material due to a change in microstructure during a fatigue test was determined from the deterioration of the stiffness of material (resilient modulus). After the trafficking of each slab, cores were taken from both outside and inside of wheel path to determine the resilient modulus. The resilient modulus of cores from outside of wheel path indicated the resilient modulus before the application of load and resilient modulus of cores from inside wheel path indicated the resilient modulus after the application of load. Resilient moduli were determined at two different temperatures, 20^{o}C and 25^{o}C. The resilient modulus at particular test temperature was then determined from the interpolation of the data. Voids in Total Mix (VTM) were also determined for each core using vacuum saturation method [**31**]. **Table 10.3** shows the resilient modulus values of cores from the different slabs before and after application of load. All of the slabs (excepting Slab L) show reduction of resilient modulus values due to loading.

Table 10.3: Change of Resilient Modulus Due to MMLS3 Loading

Slab ID	M_R Before Load (MPa)	M_R After Load (MPa)	Average Test Temp, ^oC	Applied No. of Loads
J	1880	1533	21.0	634880
K	1566	1378	24.0	279018
L	2547	2309	21.0	1440060
N	2586	1703	21.0	44800
P	2158	1629	26.0	393932

M_R – resilient modulus

10.6 Observation of Cracks

Formation of cracks as an indicator of cohesive failure of HMA was also observed and measured at different levels of load application. A typical crack formation observed is shown in **Figure 10.5(a)**. Digital photographs of wheel path were taken at different load applications. A grid formed by squares of unit cm square area was laid on the digital image of trafficked area between two strain gauges situated at two extreme ends of wheel path. A unit square area was regarded as failed area if a crack or part of a crack was present in that area. The percentage of such squares in the wheel path area gave the percentage of crack in a particular load application. **Figure 10.5(b)** shows the variation of percentage of cracks over different levels of load applications for different test slabs. Around 35 percent of the wheel path area was cracked for all slabs (excepting Slab L) at final load application.

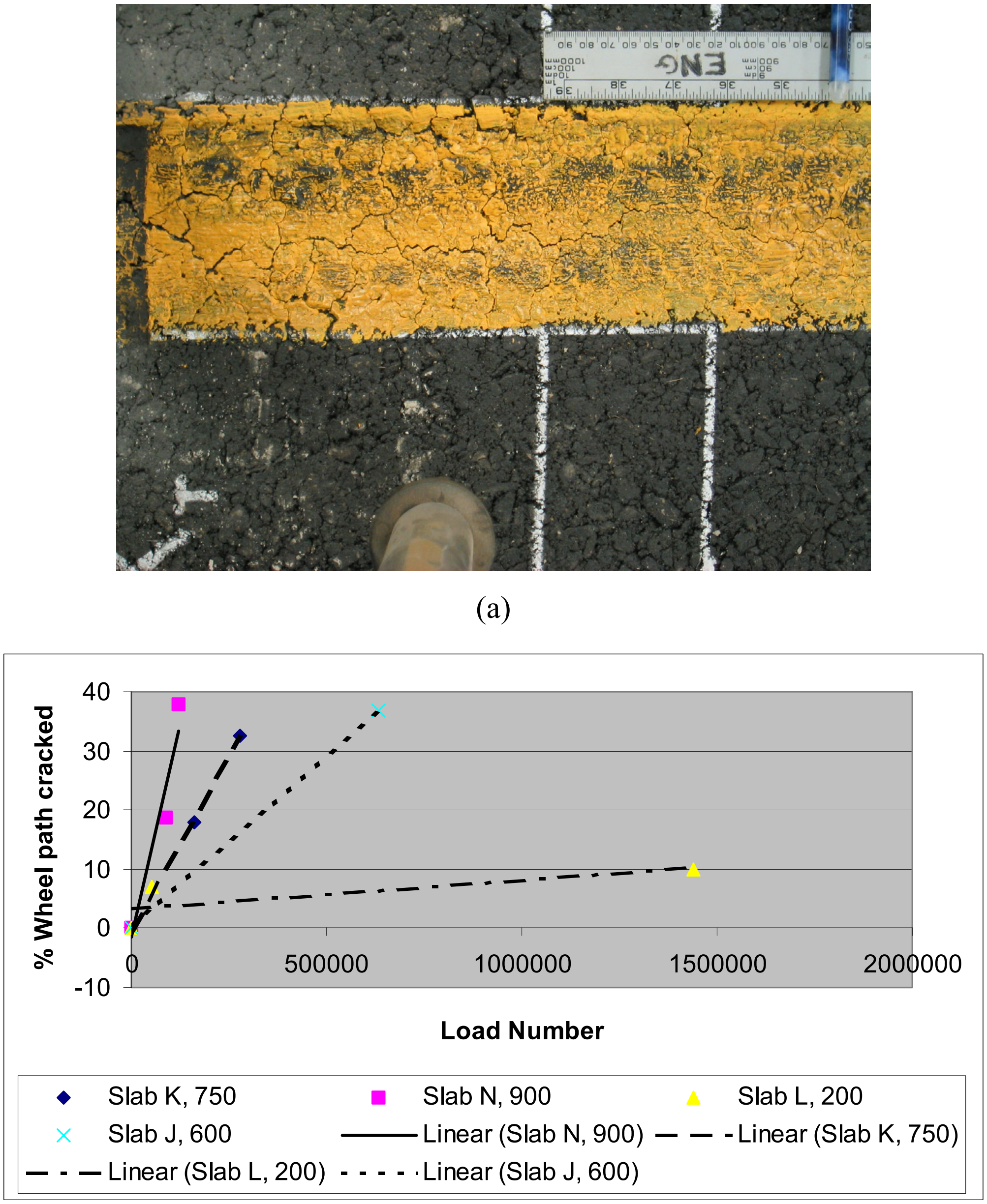

(a)

(b)

Figure 10.5: (a) Photograph of cracks formed on top of HMA test slab, (b) Increase in crack length due to traffic

10.7 Failure Load Versus Strain Relation - Discussion

The use of strain gauges in two directions allowed the development of phenomenological equations representing fatigue characteristics of HMA in (1) transverse direction and (2) longitudinal direction separately. The strain values obtained from four transverse strain gauges and four longitudinal strain gauges were averaged to obtain a pair of transverse and longitudinal strain values for each slab. It can be seen from **Table 10.1** that Slab K, P and Q were tested at considerably higher temperature than the target value (20°C), while the others showed a range of temperatures between 15°C to 20°C. Therefore, only those slabs were selected, for which temperatures were within the target value. The failure load values for longitudinal and transverse strain gauges were then plotted separately against the corresponding strains to obtain two different curves. The coefficients were calculated by performing the least square analysis of data to obtain the phenomenological equation of the form: $N_f = k_1 \varepsilon^{-k_2}$, where, k_1 and k_2 are regression constants, N_f is the number of loads to failure and ε is the initial strain. The equations obtained for transverse and longitudinal direction are:

$$N_f = 1.0 \times 10^{12} \varepsilon^{-2.5726},\ R^2 = 0.5785, \quad \text{for transverse strain gauges} \qquad (10.1)$$

$$N_f = 1.0 \times 10^{12} \varepsilon^{-2.7031},\ R^2 = 0.8624, \quad \text{for longitudinal strain gauges} \qquad (10.2)$$

The best fitted curves through the data points for both longitudinal and transverse strain gauges are shown in **Figure 10.6** along with the data points. The **Figure 10.6** also shows one more set of data points referred as "AI Data Points" which are discussed in the section "Comparison With Beam Fatigue Curves and Observations".

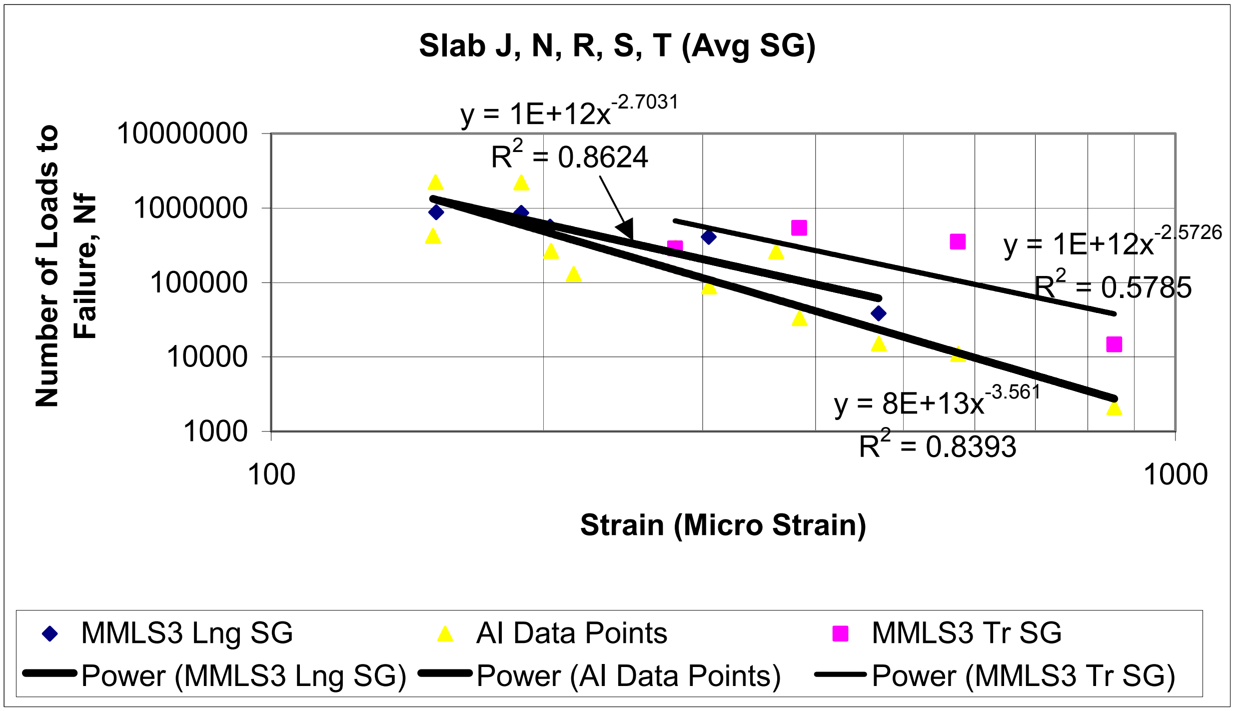

Figure 10.6: Failure load versus initial strain relations

A number of important questions need to be answered at this point:

(1) Since MMLS3 applies more realistic wheel load, as compared to beam fatigue test, how do the above equations (**Eq. 10.1** and **Eq. 10.2**) compare with those obtained from conventional beam fatigue test.

(2) In conventional analysis, as done on results from beam fatigue tests, considerations of difference between transverse and longitudinal strain gauges are not made. However field observations indicate that in most cases longitudinal cracking to be more prevalent than transverse cracking. Longitudinal cracking results from transverse strain – hence it is important to understand the difference and the cause of the difference between the fatigue equations developed on the basis of longitudinal and transverse strain.

These questions were answered through analysis and discussed in the following sections.

Comparison With Beam Fatigue Curves and Observations:

Failure load values obtained from MMLS3 tests have also been compared with N_f values calculated according to the Asphalt Institute (AI) constant stress method for determination of failure load [**32**]. To apply the equation for AI method, values of dynamic modulus |E*| were first obtained using AI formula [**32**]. Then the N_f values were calculated using average strains for each slab. Both average longitudinal and transverse strains were used to calculate AI data points because AI curve is based on beam fatigue tests, which do not distinguish between transverse and longitudinal strain gauges. **Figure 10.6** shows the position of data points obtained from AI equations as well as best-fit curve through the data points. The equation obtained using AI method is:

$$N_f = 8.0x10^{13}\varepsilon^{-3.561},\ R^2 = 0.8393 \qquad (10.3)$$

Several points can be noted from **Figure 10.6**:

1. The MMLS3 fatigue curves give higher values of failure load than the values given by AI curve. This difference exists in spite of shift factors already incorporated in the AI curve. The higher value of MMLS3 equation is reasonable because beam fatigue test, which is the basis of AI equation, does not consider actual field conditions in terms of loading, pavement structure and rest periods. This observation leads to the conclusion that MMLS3 can be used for better fatigue characterization of HMA in the laboratory than beam fatigue tests.

2. At lower strains the MMLS3 curve for longitudinal strain gauges and AI curve approach to each other and the difference between them increases with increase in strain. This is shown in **Figure 10.7** where the ratio between N_f values obtained from MMLS3 equation (longitudinal) and AI equation is plotted against different values of strains.

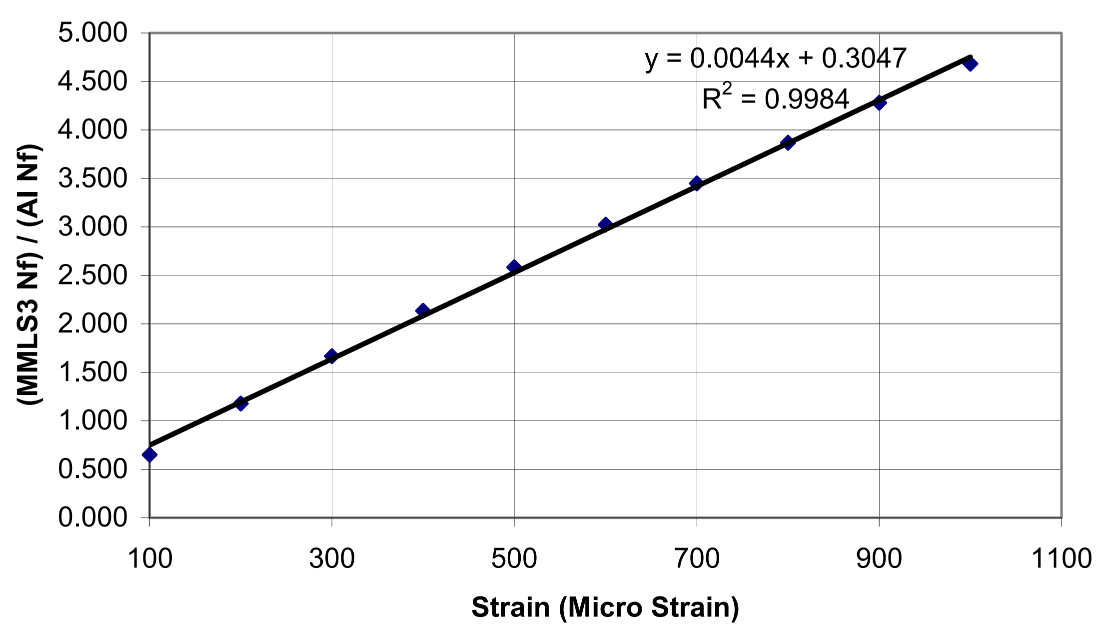

Figure 10.7: Difference between MMLS3 curve and AI curve

3. Although the MMLS3 test is a constant stress test, slope of the curve for transverse strain gauges is different from the slope of the curve for longitudinal strain gauges. **Figure 10.6** also shows that the slopes of MMLS3 curve (longitudinal) and AI curve are different. The reason for the difference in slopes among curves is not clear. However, difference in slope between MMLS3 longitudinal curve and AI curve can be due to the fact that the former is based on longitudinal strains and later is based on both longitudinal and transverse strains. There were two parameters, which varied from slab to slab during the tests: (a) the temperature was between 15°C to 20°C and (b) the modulus values of different slabs were different due to differences in compaction of the respective slabs. Since each curve in **Figure 10.6** was drawn based on data of different test slabs, this could have contributed to the differences in slopes.

4. The data points for transverse strain gauges show high scatter (R^2 = 0.5785) compared to the data points for longitudinal strain gauges (R^2 = 0.8624) and AI equation (R^2 = 0.8393). This scatter also puts the curve obtained from transverse

strain gauges above the curve from longitudinal strain gauges, which is unrealistic, since transverse strains were always higher than longitudinal strains in all cases. This indicates that in spite of the presence of the factors listed above in (iii), there are other factor(s), which is (are) affecting the behavior of the transverse strain gauges. This requires a close inspection of the behavior of transverse strain gauges throughout the test duration. As discussed in **Section 10.2.1**, the transverse strain gauges recorded higher strains due to presence of permanent irrecoverable strains and these irrecoverable strains were higher at higher temperature. Therefore, the effect of permanent strains in transverse direction should be investigated more thoroughly. This is explained in more detail in the following section.

10.8 Observation of Rutting

Loadings with the MMLS3 resulted in some amount of rutting in the model pavements. Since the dimensionality principle states that any deformation occurring in scaled pavements should be multiplied by the scale factor (3.85 for current MMLS3 tests) to obtain the field deformation, and rutting and fatigue occur simultaneously, it was decided to investigate the effect of rutting on fatigue performance. The rut depth at center of the test slabs is presented in **Figure 10.8(a)** as function of load number. As can be seen from **Figure 10.8(a)**, the maximum rut depth is 2.6 mm at the center of the test slab. Rut depth of around 5 mm at the wheel entrance end of the slabs has been observed due to the high contact pressure at the point where the wheel first touched the slab surface. A typical rutted surface is shown in **Figure 10.8(b)** and a typical cross sectional view of slab is shown in **Figure 10.8(c**) with initial and final profile. Note the heaving on both sides of wheel path and rutting inside wheel path.

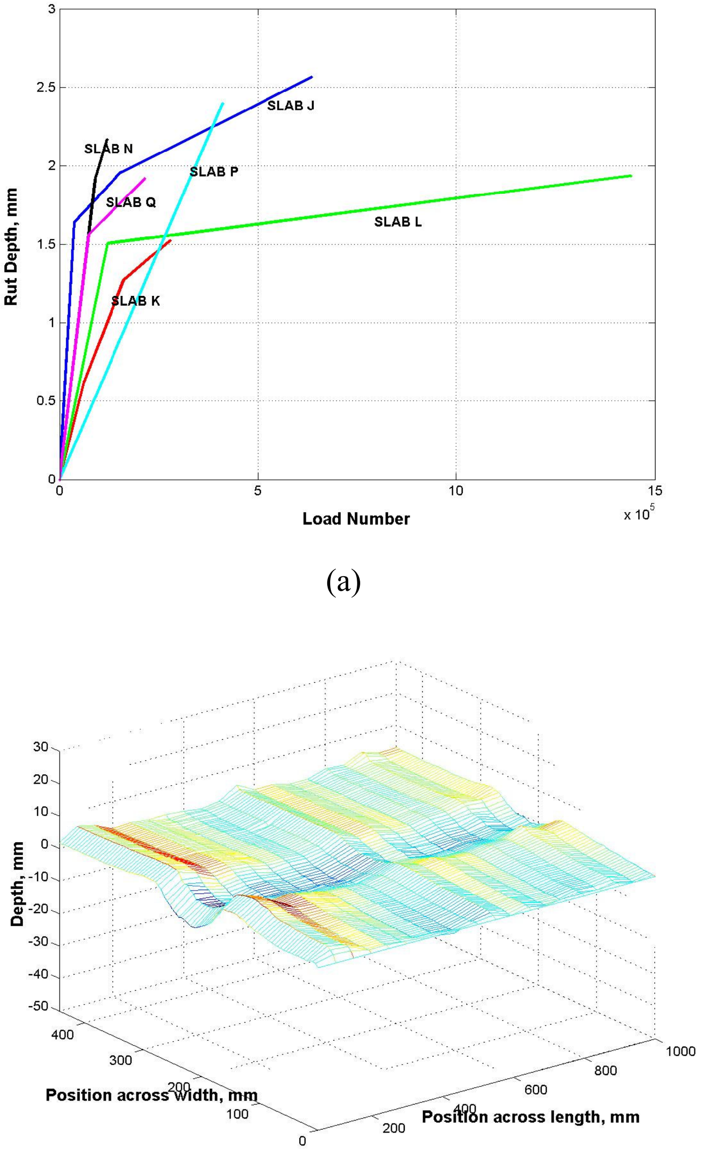

(a)

(b)

Figure 10.8: (a) Rut depth versus load number. (b) Typical rutted surface of test slab.

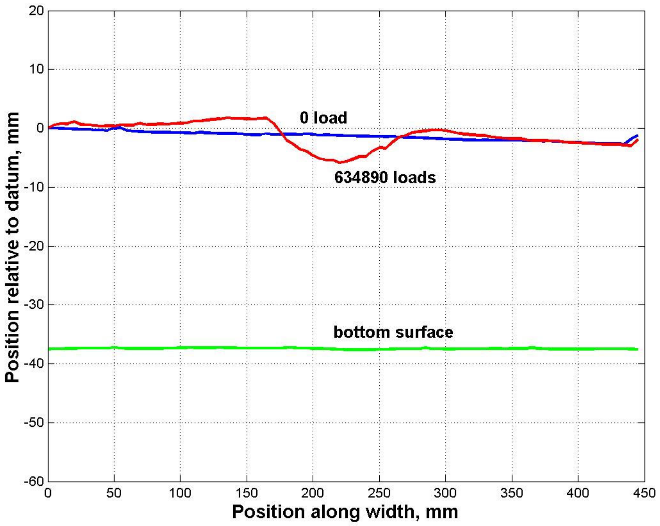

(c)

Figure 10.8 (c): Typical cross sectional view of test slab before and after traffic.

Rutting is the cause of shear deformation of HMA under the wheel path, which causes the material to be pushed away from the wheel path to both sides. This flow of material occurs in all direction under the wheel path. On the other hand, fatigue damage occurs due to repeated loading and associated dynamic strain directly under the wheel path.

It is hypothesized that fatigue failure is not only affected by repeated loading and associated dynamic strain, but also by permanent strain caused by shear deformation. The importance of this hypothesis is as follows:

(1) In the real pavements, the fatigue (or rutting) does not occur alone. Both rutting (small or significant) and fatigue damage occur from the day a new pavement is opened to traffic. Yet, in conventional analysis, rutting and fatigue are treated separately.

(2) The maximum rut depth of 2.6 mm in MMLS3 corresponds to a rut depth of 2.6 × 3.85 = 10.0 mm in field. For rutting to be significant, a rut depth of 6 mm is considered to be critical [**33**]. This critical depth of 6 mm is considered from the point of view of

deformation as well as hydroplaning potential. Therefore, 10.0 mm rut depth in field can affect fatigue characteristics of the mix considerably.

The above points were investigated by performing tests and analysis in the following sections.

Approach #1:

If we can measure the horizontal strain outside the wheel path as well as inside wheel path, we can have an idea of how much strain is attributable to rutting. This strain would be the horizontal component of the three dimensional strain caused by material flowing in all three directions. To achieve this, one needs continuous acquisition of data from inside wheel path as well as from outside wheel path. Since transverse strain gauges generally failed quite early due to high strain, Linear Variable Displacement Transducers (LVDTs) were used to determine strain both inside and outside wheel path for Slab P and Slab Q.

For both slabs, three neoprene layers (each of thickness 25 mm) of size same as the size of the mold were placed. An additional neoprene layer of thickness 25 mm and size same as the test slab was put directly under the slab. Two pairs of LVDTs were used, one at 20 mm from centerline and other at 50 mm from the centerline. Therefore, the first pair is used to measure strain directly under wheel path over 40 mm length and the second pair at the outside wheel path is used to measure strain over 100 mm length. The LVDTs used were of length 10 mm with range +/- 5 mm. For slab P, the first slab with LVDT, the readings from LVDTs were found to be increasing with increase in time, but in the +5 direction, which indicated a problem with the LVDT setup. Upon investigation, it was found that, since LVDT was fixed inside the groove underneath the slab and glued to the bottom surface of slab P, the movement of slab affected the movement of LVDT and as a result, release of strain occurred. This problem was solved in the next slab, slab Q, by not gluing the LVDT to the slab; rather it was fixed outside separately and independently of the slab, so that movement of slab did not affect the movement of LVDT. This was done by making a groove on top of the neoprene layer and also under the slab such that the total thickness of the groove was slightly more than the total diameter of LVDT casing. **Figure 10.9** shows the positions of LVDT with the acquisition system. The LVDT was placed on top of a spacer, which separated the LVDT casing from touching the rubber. The top of the LVDT casing was free from touching the underside of the slab, thus ensuring no contact with either slab or rubber. The LVDT was fixed at the outside of the slab by bolting to a wood board, which was fixed on the frame of the mold.

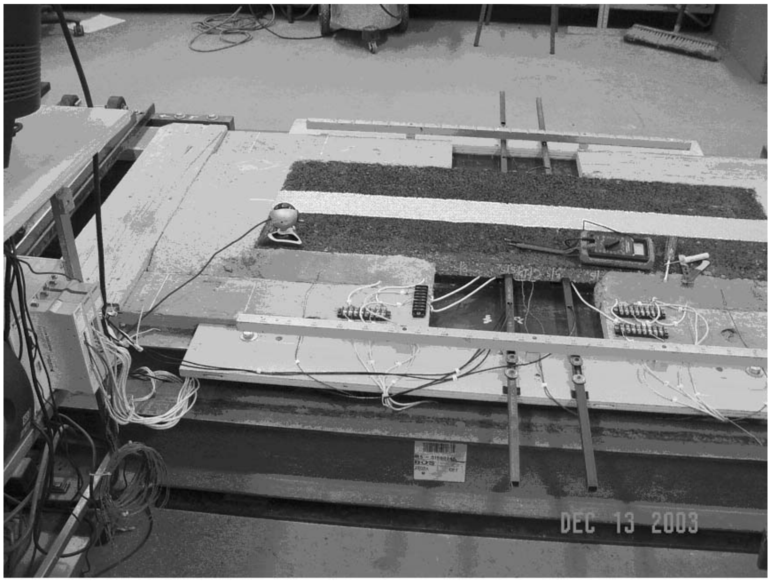

Figure 10.9: LVDT positions (Slab Q) along with acquisition system.

The average strain recorded by strain gauges is shown in **Figure 10.10(a)**. The average strain obtained from LVDT reading is shown in **Figure 10.10(b)**. Note that, LVDTs 1 and 2 were placed 40 mm apart and LVDTs 3 and 4 were placed 100 mm apart. The average strains recorded by LVDTs show a steady increase for LVDTs placed outside wheel path.

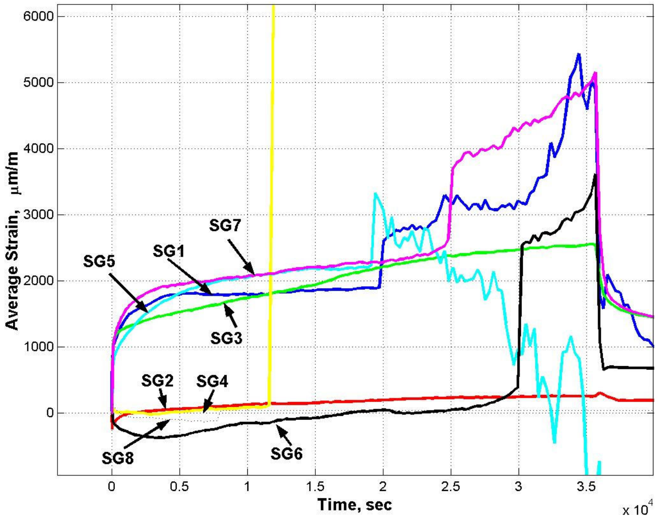

(a)

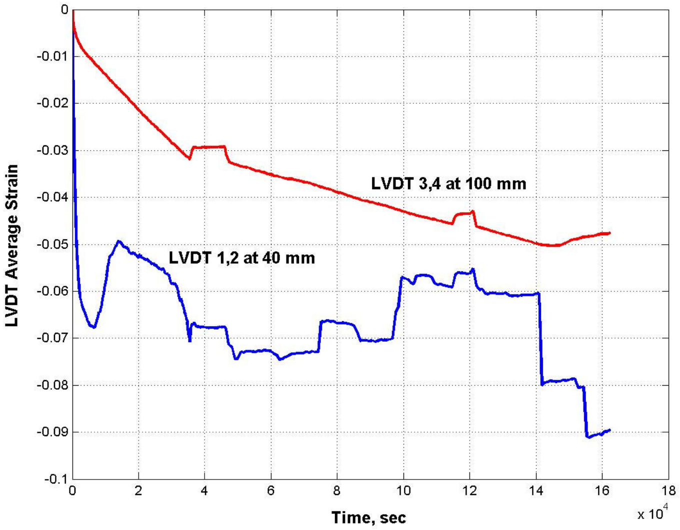

(b)

Figure 10.10: (a) Average strain from SG for Slab Q. (b) Average LVDT strain from Slab Q.

Figure 10.10(b) also shows that average strains recorded by LVDTs are much higher than the same recorded by strain gauges. The same thing is observed for resilient strain when we compare resilient strain recorded by strain gauges (**Figure 10.11(a)**) and the same recorded by LVDTs (**Figure 10.11(b)**). One possible reason is that the LVDTs measured the movements of particles, whereas the strain gauges most likely measured surface strains.

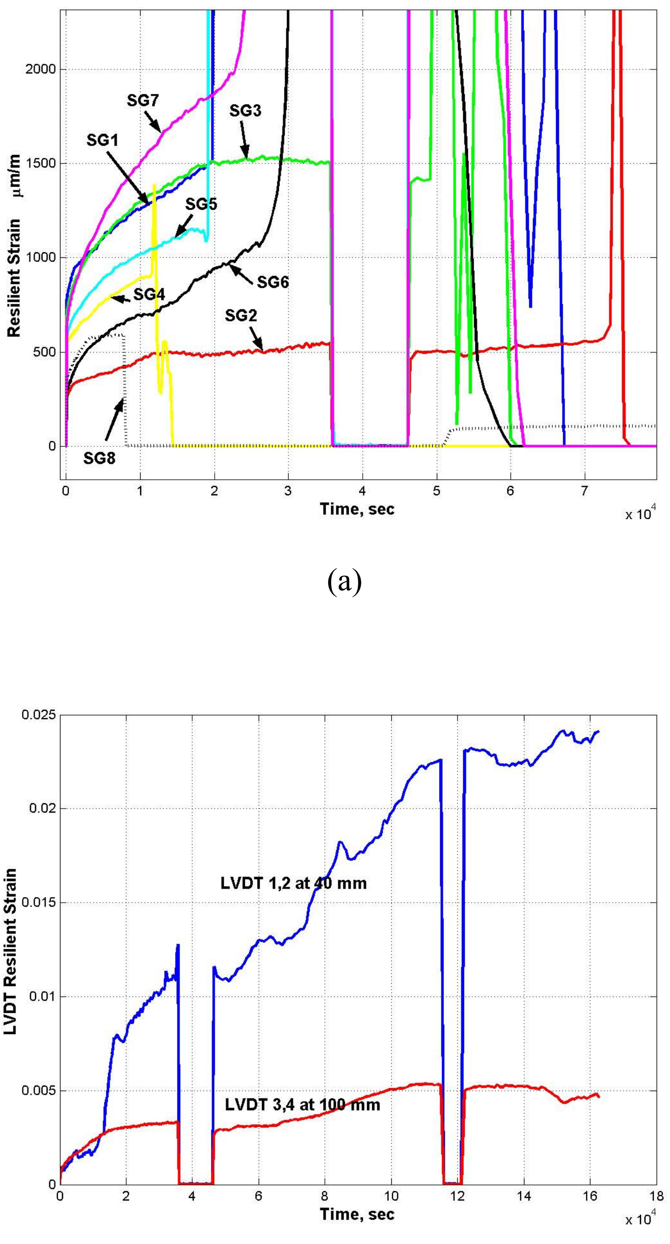

(a)

(b)

Figure 10.11: (a) Resilient strain from strain gauge for Slab Q. (b) Resilient strain from LVDT for Slab Q.

Therefore, following conclusions can be drawn from the results obtained from LVDT:

(1) Rutting and fatigue occur simultaneously and we need to consider the effect of both on fatigue behavior of HMA.

(2) The results indicated that although maximum rut depth was below 3 mm, considerable movement of particles due to shear deformation was observed (**Figure 10.8(c)**).

Approach #2:

To investigate the behavior of rutting and the associated readings of the LVDTs, rutting data were analyzed in detail for each of the slabs tested. As mentioned earlier, surface profiles of each of the slabs were taken at certain interval of times during loading, with initial profile at the beginning of the test. The profile of the supporting Neoprene layer was also taken so that a complete thickness profile was obtained for each slab. The profiles were taken at intervals of 50 mm along the length of the slab with 5 mm interval along the width of the slabs. As can be seen from **Figure 10.8(c)**, rutting caused reduction in thickness. **Table 10.4** shows the VTM of samples at start and end of loading. It can be seen from **Table 10.4** that there is a decrease in VTM due to traffic.

Table 10.4: Initial and Final Air Voids in Different Slabs

Slab ID	**Initial Void in Total Mix (%)**	**Final Void in Total Mix (%)**
J	9.97	6.18
K	9.08	7.71
L	13.53	11.49
N	11.47	10.6
P	10.06	8.63

To get a quantitative measurement of flow of material, amount of materials inside wheel path before traffic and after traffic have been calculated for each slab. To calculate this, the specific gravity values and volume of material inside wheel path before and after traffic have been used. Once the material transferred outside the wheel path was calculated, the associated strain was determined. This was done by converting the transferred mass into volume using specific gravities (after traffic) and then converting the volume into deformation in horizontal direction. The subsequent strain was calculated over the length of 80 mm wheel path. **Table 10.5** shows a typical calculated percent of mass transfer from wheel path, percent change in thickness and associated strain. It is interesting to note that calculated horizontal strains are in the order of observed strains in LVDTs, thus, confirming that LVDTs were indeed recording movements due to mass transfer due to flow. Therefore, it can be said that, higher permanent strain recorded by transverse strain gauges compared to longitudinal strain gauges was partly due to dynamic effect from wheel and partly from mass movement from inside to outside wheel path. Since fatigue life is associated with resilient dynamic strain only, the presence of permanent strain due to rutting affects fatigue life of pavement. This particular aspect of pavement behavior should be investigated further.

Table 10.5: Typical Horizontal Strain Distribution Along Length Due to Rutting

Position along length, mm	**Percent mass transfer**	**Percent thickness change**	**Calculated horizontal strain, μm/m**
50	5.362	6.83	6.02E+04
100	3.833	5.325	4.24E+04
150	3.254	4.754	3.57E+04
250	-2.827	-1.232	-2.92E+04
300	2.043	3.563	2.22E+04
350	3.394	4.893	3.73E+04
450	2.537	4.049	2.77E+04
500	3.333	4.833	3.66E+04
550	2.89	4.397	3.16E+04
600	3.127	4.63	3.43E+04
650	4.28	5.765	4.75E+04
750	2.587	4.099	2.82E+04
800	2.757	4.266	3.01E+04

Table 10.5: Typical Horizontal Strain Distribution Along Length Due to Rutting (Cont.)

Position along length, mm	**Percent mass transfer**	**Percent thickness change**	**Calculated horizontal strain, μm/m**
850	1.822	3.345	1.97E+04
900	3.416	4.915	3.76E+04
950	3.224	4.726	3.54E+04
1000	2.269	3.785	2.47E+04
50	5.362	6.83	6.02E+04
100	3.833	5.325	4.24E+04
150	3.254	4.754	3.57E+04

10.9 Effect of Temperature Gradient on Strain Response

In this present study, the viscoelastic behavior of HMA is assumed to be linear. Being viscoelastic, the response of HMA is affected by temperature. In the present study, the target temperature was chosen to be 20^{o}C. As discussed in **Section 10.4**, in many situations it was difficult to keep the temperature constant at the target temperature due to various reasons. Temperature varied considerably during the tests, as it is evident from plots in **Figure 10.3(b), (c)**, where temperature is plotted against time. It has been mentioned in **Section 10.7** that fatigue characteristics curves were drawn based on strain data obtained from slabs, which showed temperature variation within 15^{o}C to 20^{o}C. This variation of five degrees Celsius was assumed to be reasonable having no considerable effect on fatigue performance of HMA being tested. Therefore, no analysis was performed on these data to apply any temperature correction factor. However, the comparison of data from Slab K, P and Q, which showed non-uniform temperature variation during the tests, with the data from other slabs with relatively uniform temperature variation shows many important facts of dependence of strain on temperature. These are explained in the following paragraphs in more details.

The temperature variation of Slab J and K is shown in **Figure 10.3(a)** and **10.3(b)**. As it can be seen from the plots, Slab J had a uniform temperature variation, while Slab K had a variation with temperature gradient, making them ideal candidate for comparison. For comparison purpose, SG5 (transverse) and SG6 (longitudinal) of Slab J, SG3 (longitudinal) and SG4 (transverse) of Slab K and SG6 (longitudinal) and SG7 (transverse) for Slab Q are chosen. These strain gauges were selected because of the following reasons:

(a) They worked well during secondary phase of strains.

(b) They were not positioned at the edge of the slabs where wheel entered, therefore, eliminating the effect of high contact stress of wheel.

(c) They had comparable initial resilient strains:

SG5 of Slab J (Transverse): 625 με
SG6 of Slab J (Longitudinal): 341 με
SG4 of Slab K (Transverse): 664 με
SG3 of Slab K (Longitudinal): 323 με
SG7 of Slab Q (Transverse): 630 με
SG6 of Slab Q (Transverse): 290 με

The gradient of resilient strain time history of the strain gauges during the secondary phase of each history is calculated and tabulated in **Table 10.6** along with the gradient of temperature history for the same time duration. It can be seen from **Table 10.6** that gradient of secondary phase of strains is increased with increase in the gradient of temperature.

Table 10.6: Effect of temperature gradient on strain

Strain, με	**Gradient of Strain, με/300 sec**	**Gradient of Temp, ^{o}C/300 sec**
625	0.300	0.000
341	0.075	0.000
664	3.000	0.015
323	4.000	0.015
630	10.000	0.045
290	7.500	0.060

The important conclusion, which can be drawn from the above discussion, is that: strain at any time is a function of temperature and gradient of temperature variation. This indicates that damage can occur more quickly than anticipated if temperature gradient is not taken care of during the test. If there is temperature gradient present, care must be taken to interpret the strain observed by applying suitable temperature correction factors incorporating the two effects: temperature and gradient of temperature at that point.

10.10 Analysis of MMLS3 Model Pavement Using Finite Element Method

Since models of test pavement used in this study contain Neoprene (rubber), which is a hyperelastic material and the boundary conditions are different from semi-infinite boundary conditions assumed in elastic layer analysis, the stresses and strains could only be determined by numerical methods. For this purpose, the general purpose finite element software ABAQUS Standard® [**34**] was used to develop several models of pavement under MMLS3 and full-scale pavements and effect of layer thickness were investigated for both cases under static loading from tire pressure. Although the assumptions of elastic homogeneous isotropic material properties for all layers and static pressure distribution deviated from actual experimental conditions, the effect of thickness variation on strains was successfully simulated in the finite element models. The model parameters used in the analysis are explained below.

The mold used in the MMLS3 testing in this study consisted of four layers: (1) a top HMA layer of variable thickness (17 mm, 25 mm and 50 mm), (2) three layers of Neoprene rubber of grade D60 or D80, each 25 mm thick, (3) one 16 mm thick steel plate and (4) 214 mm thick layer of sand. In the finite element model, the HMA layer, steel plate and sand layer were modeled as linear elastic material and the Neoprene layer was modeled as nonlinear elastic (hyperelastic) material. The elastic properties of HMA were obtained from the results of resilient modulus test data for untrafficked cores. The Young's moduli and Poisson's ratios used were 200 GPa and 0.26 for steel (assumed) and 35 MPa (determined from tests with a Geogauge) and 0.40 (assumed) for sand. Uniaxial stress/strain data for rubber material determined in the laboratory was used for hyperelastic model of rubber. The tire pressure of 690 kPa was assumed to be distributed uniformly on a square area with total load of 2.7 kN. The typical finite element mesh of MMLS3 model pavement is shown in **Figure 10.12**.

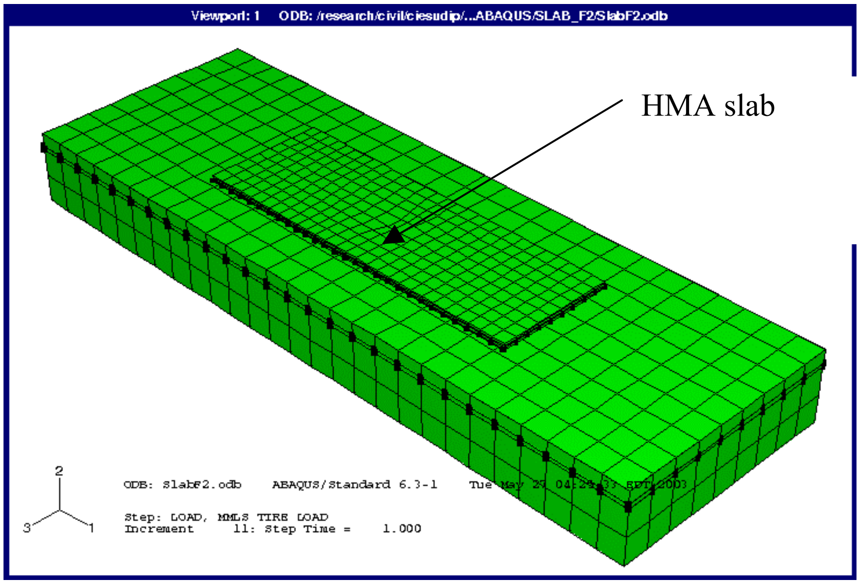

```
ODB: SlabF2.odb    ABAQUS/Standard 6.3-1    Tue May 27 04:24:37 EDT 2003

Step: LOAD, MMLS TIRE LOAD
Increment     11: Step Time =    1.000
```

Figure 10.12: Finite element mesh model of MMLS3 model pavement.

All degrees of freedom at bottom and sides of rubber, steel and sand layers were modeled as fixed since they were inside the mold and free degrees of freedoms were assigned to the sides of HMA slab. A tied contact surface was assumed between the HMA slab and the rubber layer. Contour of logarithmic strain computed at the element integration points along the longitudinal direction at top and bottom of the HMA slab are shown in **Figure 10.13(a)** and **Figure 10.13(b)** respectively.

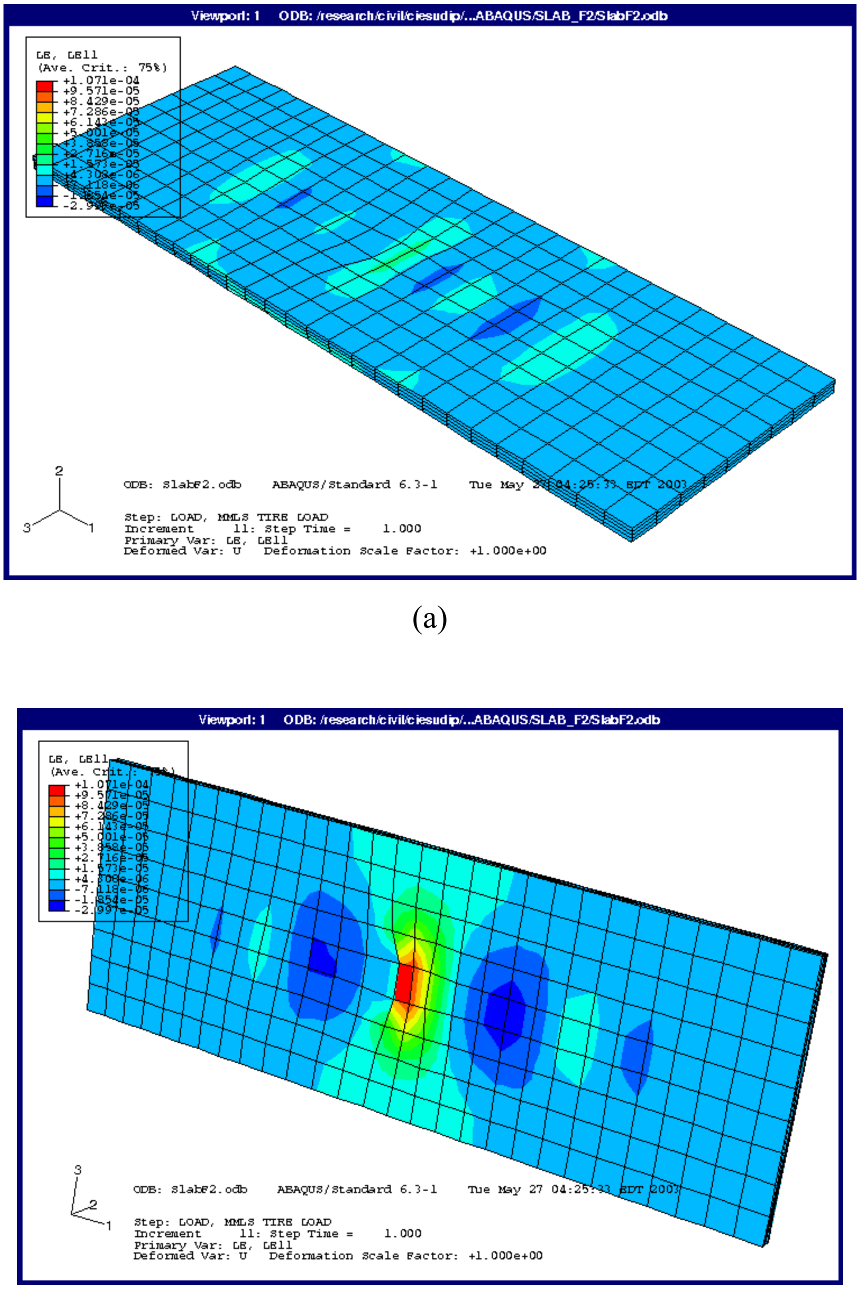

(a)

(b)

Figure 10.13: (a) Longitudinal strain contour at top of HMA slab (b) Longitudinal strain contour at bottom of HMA slab

It can be seen from the plots in **Figure 10.13(a)** and **Figure 10.13(b)** that strain at the top is compressive and strain at the bottom is tensile, which simulates the actual situation in field. Moreover, the strain at a position just outside of the wheel-loaded area is compressive, which is also in agreement with actual field situation.

The directions of principal strains below the loaded area at the bottom of HMA slab are plotted in **Figure 10.14**. It can be seen from **Figure 10.14** that maximum principal strains occur mostly in the transverse direction. Since, fatigue crack growth occurs normal to the direction of maximum principal strains, it seems that for MMLS3, fatigue crack can develop along longitudinal direction along wheel path (which has been observed in typical MMLS3 test).

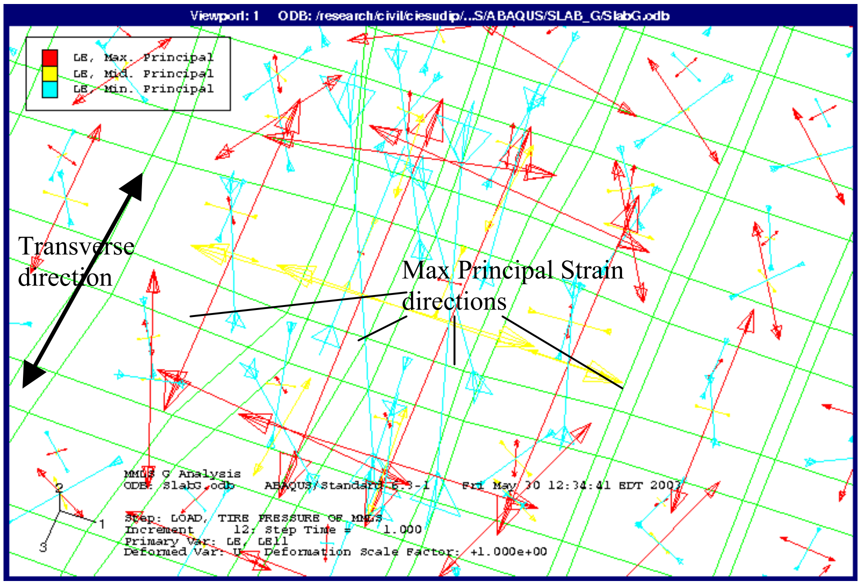

```
MMLS G Analysis
ODB: SlabG.odb    ABAQUS/Standard 6.3-1    Fri May 30 12:34:41 EDT 2003

Step: LOAD, TIRE PRESSURE OF MMLS
Increment     12: Step Time =     1.000
Primary Var: LE, LE11
Deformed Var: U   Deformation Scale Factor: +1.000e+00
```

Figure 10.14: Direction of principal strains under model pavement.

10.11 Analytical Model of MMLS3 Model Pavement

The finite element model presented in **Section 10.10** is based on the elastic analysis. The results obtained from FEM analysis can be used as response at initial conditions of loading where the response can be assumed to be elastic. During the cyclic loading, both transverse and longitudinal strain increased. Therefore, it was necessary to have an analytical model, which can simulate this time dependent behavior. The development of the analytical model had two objectives:

(a) To model the time dependent behavior and

(b) To control several test parameters by performing a parametric study before the start of a new test.

For this purpose, the test slab was modeled as viscoelastic simply supported plate on elastic foundation and the time dependent response was analyzed. The following assumptions were made in this analysis: (a) vehicle-pavement dynamic interaction (plate vibration) is negligible and (b) the time dependence is due to the time dependent material behavior (viscoelastic). Each pass of axle load was suitable modeled as periodic loading and subsequently elastic viscoelastic corresponding principle was used to obtain the viscoelastic solution.

10.11.1 Modeling Wheel Load:

MMLS3 loading consisted of a repeated moving load over the length of the pavement from one direction. Thus, the load traversed a distance equal to the length of test slab in certain time depending on velocity. The position of load, Y_{LOAD}, at any point of time on the plate can be written as: $Y_{LOAD}(t) = Vt$, where, V is the velocity. Therefore, if the load has a period T, the position during any p th cycle of load can be written as:

$$Y_{LOAD}(t) = V(t-(p-1)T), \text{ for } (p-1)T \leq t < pT \tag{10.4}$$

This is represented in **Figure 10.15**, where $Y_{LOAD}(t)$ has been plotted against t.

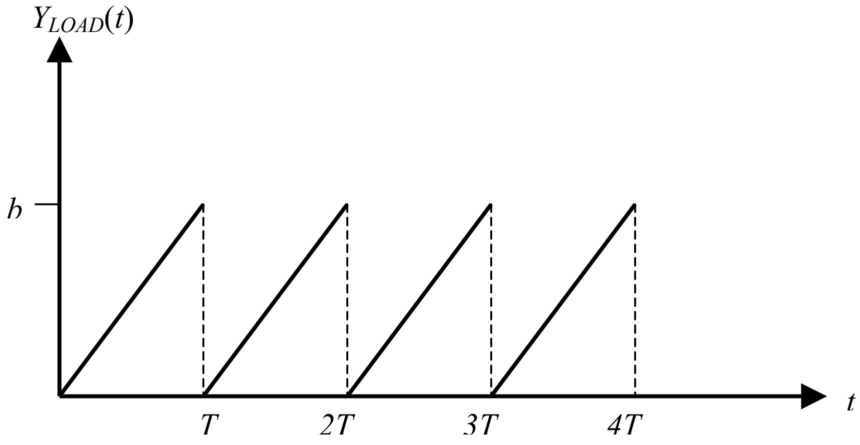

Figure 10.15: Periodic loading of MMLS3

10.11.2 Modeling Test Slabs

In order to calculate the strain underlying the slab, it is required that the interaction of slab and the underlying material be modeled in appropriate way so that the physical behavior is represented in the mathematical model. For this purpose, the slab can be viewed as a thin plate sitting over a flexible foundation and subjected to a traction force on the surface of plate over a rectangular region, as shown in **Figure 10.16**.

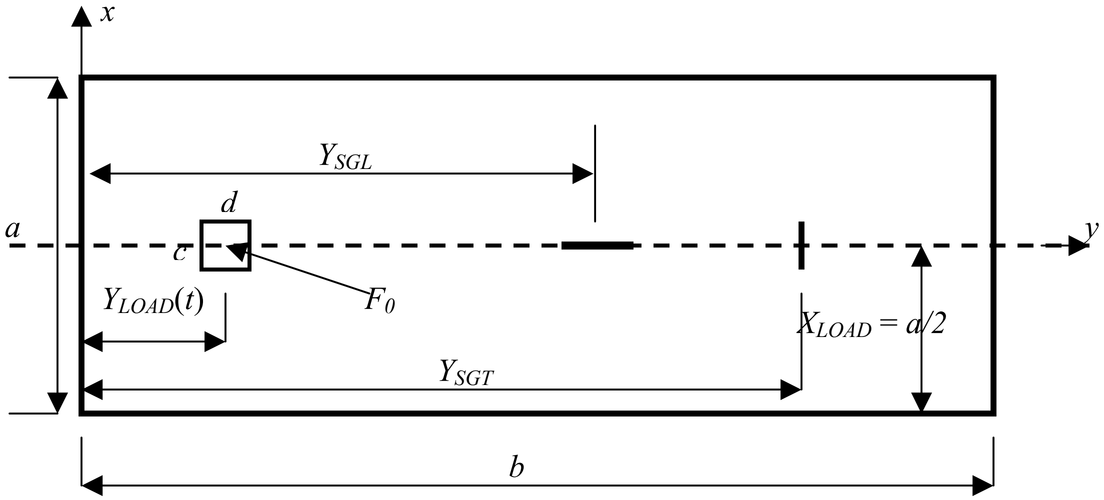

Figure 10.16: Slab dimensions and relative positions of strain gauges and load

In **Figure 10.16**, position of load (X_{LOAD}, Y_{LOAD}) is shown along with the positions of strain gauges, Y_{SGT} (transverse) and Y_{SGL} (longitudinal). The length and width of the slab are shown as *a* and *b*. The load acts over a small rectangular area of size *c* x *d* with amplitude F_0. The axis system runs parallel to the edges of the plate as shown in the figure.

Assuming small deformation behavior, the equilibrium equation of the plate can be written as:

$$\begin{aligned}
&\frac{\partial^4 w}{\partial x^4}+2\frac{\partial^4 w}{\partial x^2 \partial y^2}+\frac{\partial^4 w}{\partial y^4}=\frac{p-Kw}{D}\\
&p=p(x,y)\\
&w=w(x,y)\\
&D=\frac{Eh^3}{12(1-\upsilon^2)}
\end{aligned}\tag{10.5}$$

where, *w* is the vertical deformation, *h* is the thickness of the plate and *K* is the stiffness of the underlying layer. Both *w* and traction *p* are function of special coordinates and time. The vertical deformation w is obtained as solution of the above differential equation subject to the proper boundary conditions.

If the traction force is constant over a certain area on the surface of the slab, it can be written in the form: $p(x,y)=\frac{F_0}{cd}$, where, a traction force of F_0 is distributed over an area *cd* on the surface of the slab. We relate F_0 with the traction force of tire of MMLS3, with F_0 = 2.7 kN. To obtain the exact form of *w*(*x,y*), we solve the above differential equation subjected to the simply supported boundary condition at all sides of the slab. The solution is readily available in literature and obtained by expanding *p*(*x,y*) and *w*(*x,y*) in Fourier series, giving the following form of *w*:

$$\begin{aligned}
&w(x,y)=\sum_{m=1}^{\infty}\sum_{n=1}^{\infty}a_{mn}\sin\frac{m\pi x}{a}\sin\frac{n\pi y}{b}\\
&a_{mn}=\frac{p_{mn}}{\pi^4 D\left[\left(\frac{m}{a}\right)^2+\left(\frac{n}{b}\right)^2\right]^2+K}\\
&p_{mn}=\frac{4F_0}{abcd}\int_{X_{load}-c/2}^{X_{load}+c/2}\int_{Y_{load}-d/2}^{Y_{load}+d/2}\sin\frac{m\pi x}{a}\sin\frac{n\pi y}{b}\,dxdy
\end{aligned}\tag{10.6}$$

where, $p(x,y)$ is defined over the interval $X_{LOAD}-c/2 \le x \le X_{LOAD}+c/2$ and $Y_{LOAD}-d/2 \le y \le Y_{LOAD}+d/2$ and a and b are the length of the sides of the slabs. The integration yields the following form of p_{mn}.

$$\begin{aligned} p_{mn}(t) &= P_{mn}\sin\left(\frac{n\pi V}{b}(t-(p-1)T)\right) \\ P_{mn} &= \frac{16F}{\pi^2 mncd}\sin\left(\frac{m\pi X_{LOAD}}{a}\right)\sin\left(\frac{m\pi c}{2a}\right)\sin\left(\frac{n\pi d}{2b}\right) \end{aligned} \tag{10.7}$$

The strains are given by: $\varepsilon_x(x,y,z,t) = -z\frac{\partial^2 w}{\partial x^2}, \varepsilon_y(x,y,z,t) = -z\frac{\partial^2 w}{\partial y^2}$. The strain gauges recorded the average strains over the length of the strain gauges. Therefore, it is required to calculate the average strain over certain length. Therefore, the average transverse and longitudinal strain at bottom of test slab ($z = h/2$) over certain length L is:

$$\begin{aligned} \varepsilon_x(t) &= \frac{1}{L}\int_{X_{SG}-L/2}^{X_{SG}+L/2} \varepsilon_x(x,y,t)dx \\ \varepsilon_y(t) &= \frac{1}{L}\int_{Y_{SG}-L/2}^{Y_{SG}+L/2} \varepsilon_y(x,y,t)dy \end{aligned} \tag{10.8}$$

After inserting p_{mn} (**Eq. 10.7**) into the equation of a_{mn} (**Eq. 10.6**) and performing differentiation and integration we obtain the following general periodic form of strain:

$$\varepsilon(t) = A\sum_m \sum_n \frac{a}{bE+c}P(t), \text{ for } (p-1)T \le t < pT \tag{10.9}$$

The coefficients A, a, b and c are given by:

$$b = \pi^4 h^3 \left(\left(\frac{m}{a} \right)^2 + \left(\frac{n}{b} \right)^2 \right) \qquad (10.10)$$

$$c = 12k(1 - \upsilon^2)$$

For transverse strain gauges:

$$A = \frac{1}{L} \frac{h}{2} \frac{\pi}{a} 12(1-\upsilon^2) \frac{16F}{\pi^2 cd}$$

$$a = \frac{1}{n} \sin\left(\frac{m\pi X_{LOAD}}{a} \right) \sin\left(\frac{m\pi c}{2a} \right) \sin\left(\frac{n\pi d}{2b} \right) \sin\left(\frac{n\pi Y_{SG}}{B} \right). \qquad (10.11)$$

$$\left[-\cos\left(\frac{m\pi}{2} + \frac{m\pi L}{2a} \right) + \cos\left(\frac{m\pi}{2} - \frac{m\pi L}{2a} \right) \right]$$

For longitudinal strain gauges:

$$A = \frac{1}{L} \frac{h}{2} \frac{\pi}{b} 12(1-\upsilon^2) \frac{16F}{\pi^2 cd}$$

$$a = \frac{1}{m} \sin\left(\frac{m\pi X_{LOAD}}{a} \right) \sin\left(\frac{m\pi c}{2a} \right) \sin\left(\frac{n\pi d}{2b} \right) \sin\left(\frac{m\pi}{2} \right). \qquad (10.12)$$

$$\left[-\cos\left(\frac{n\pi Y_{SGL}}{2} + \frac{n\pi L}{2b} \right) + \cos\left(\frac{n\pi Y_{SGL}}{2} + \frac{n\pi L}{2b} \right) \right]$$

and $P(t)$ is given by:

$$P(t) = \sin\left(\frac{n\pi V}{b} (t - (p-1)T) \right), \text{ for } (p\text{-}1)T \le t < pT \qquad (10.13)$$

10.11.3 The Laplace Transformed of Strain

The above form of $\varepsilon(t)$ is the elastic strain. Since we are interested in the viscoelastic strain, we use the elastic-viscoelastic corresponding principle. The Laplace transformed form of the strain is given by:

$$\bar{\varepsilon}(s) = A\sum_m\sum_n \frac{a}{bs\bar{E}(s)+c}\bar{P}(s) = A\sum_m\sum_n \frac{as\bar{J}(s)}{b+cs\bar{J}(s)}\bar{P}(s) \qquad (10.14)$$

where $\bar{P}(s), \bar{E}(s), \bar{J}(s)$ are the Laplace transformed of forcing function, tensile relaxation modulus and tensile creep compliance respectively. Here the relation $\bar{E}(s)\bar{J}(s) = \frac{1}{s^2}$ has been used. The Laplace transformed strain $\bar{\varepsilon}(s)$ can be written as product of two Laplace transformed functions as: $\bar{\varepsilon}(s) = A\sum_m\sum_n \bar{f}(s)\bar{P}(s)$, where $\bar{f}(s) = \frac{as\bar{J}(s)}{b+cs\bar{J}(s)}$. The inverse transformed is therefore:

$$\varepsilon(t) = A\sum_m\sum_n \int_0^t f(t-u)P(u)du \qquad (10.15)$$

To obtain the inverse transform of $\bar{f}(s)$, a particular form of $\bar{J}(s)$ is needed. The HMA is modeled as four parameter Kelvin model showing steady state increase in strain (Burger's model) and the associated creep compliance $J(t)$ is given by:

$$J(t) = \alpha + \beta t + \gamma(1-\exp(-\tau t)) \qquad (10.16)$$

where, α, β, γ and τ are four parameters determined from creep tests. Then $\bar{J}(s)$ is given by: $\bar{J}(s) = \frac{\alpha+\gamma}{s} + \frac{\beta}{s^2} - \frac{\lambda}{s+\tau}$. $\bar{J}(s)$ is substituted in **Eq. 10.14** and after simplifying by algebraic manipulation, the resulting equation is inverted in time domain to obtain $f(t)$.

10.11.4 The Inverse Transform *f*(*t*)

The inverse transformed *f*(*t*) is given by:

$$f(t) = A_1 Dirac(t) + A_2 \exp(B_1 t) + A_3 \exp(B_2 t) \tag{10.17}$$

where the constants A_1, A_2, A_3, B_1, B_2 are given by:

$$\begin{aligned}
A_1 &= \frac{a_1}{a_2} \\
A_2 &= \frac{1}{2}\left[\frac{b_1}{a_2} - \frac{a_1 b_2}{a_2^{\,2}} + \frac{\dfrac{c_1}{a_2} - \dfrac{a_1 c_2}{a_2^{\,2}} - \dfrac{b_2}{2a_2}\left(\dfrac{b_1}{a_2} - \dfrac{a_1 b_2}{a_2^{\,2}}\right)}{\sqrt{\left(\dfrac{b_2}{2a_2}\right)^2 - \dfrac{c_2}{a_2}}}\right] \\
A_3 &= \frac{1}{2}\left[\frac{b_1}{a_2} - \frac{a_1 b_2}{a_2^{\,2}} - \frac{\dfrac{c_1}{a_2} - \dfrac{a_1 c_2}{a_2^{\,2}} - \dfrac{b_2}{2a_2}\left(\dfrac{b_1}{a_2} - \dfrac{a_1 b_2}{a_2^{\,2}}\right)}{\sqrt{\left(\dfrac{b_2}{2a_2}\right)^2 - \dfrac{c_2}{a_2}}}\right] \\
B_1 &= -\frac{b_2}{2a_2} + \sqrt{\left(\frac{b_2}{2a_2}\right)^2 - \frac{c_2}{a_2}} \\
B_2 &= -\frac{b_2}{2a_2} - \sqrt{\left(\frac{b_2}{2a_2}\right)^2 - \frac{c_2}{a_2}}
\end{aligned} \tag{10.18}$$

10.11.5 Final form of $\varepsilon(t)$; Response During Loading

In **Eq. 10.15**, the integrations are performed over each cycle of loading. Therefore, it can be written as:

$$\varepsilon(t) = A\sum_{m}\sum_{n}\left[\sum_{j=0}^{p-2}\int_{jT}^{(j+1)T} f(t-u)P(u)du + \int_{(p-1)T}^{t} f(t-u)P(u)du\right], \text{ for } (p\text{-}1)T \le t < pT \tag{10.19}$$

The first integral in **Eq. 10.19** indicates the integration over previous cycles and the last integral is for the current cycle. Inserting the form of *f*(*t*) from **Eq. 10.17** into **Eq. 10.19** we obtain the simplified form of **Eq. 10.19**:

$$\varepsilon(t) = A\sum_{m}\sum_{n}\left[A_1P(t) + \sum_{j=0}^{p-2}\left(A_2I_1(t) + A_3I_2(t)\right) + A_2I_3(t) + A_3I_4\right], \text{ for } (p\text{-}1)T \le t < pT \tag{10.20}$$

where,

$$\begin{aligned}
I_1(t) &= \int_{jT}^{(j+1)T} \exp(B_1(t-u))P(u)du \\
I_2(t) &= \int_{jT}^{(j+1)T} \exp(B_2(t-u))P(u)du \\
I_3(t) &= \int_{(p-1)T}^{t} \exp(B_1(t-u))P(u)du \\
I_4(t) &= \int_{(p-1)T}^{t} \exp(B_2(t-u))P(u)du
\end{aligned} \tag{10.21}$$

In **Eq. 10.21**, the general integral $I(t)=\int \exp(B(t-u))P(u)du$ is evaluated as:

$$I(t)=-\frac{1}{1+\left(\frac{Bb}{n\pi V}\right)^2}\frac{b}{n\pi V}\exp(B(t-u))\left[\begin{array}{l}\cos\left(\frac{n\pi V}{b}(u-(p-1)T)\right)\\ +\frac{Bb}{n\pi V}\sin\frac{n\pi V}{b}(u-(p-1)T)\end{array}\right], \quad (10.22)$$

for $(p\text{-}1)T \le t < pT$

From **Eq. 10.22**, the integrals are calculated by inserting appropriate limits. The response at transverse strain gauge located at *y=b/4* from wheel end due to single pass of load is shown in **Figure 10.17**. **Figure 20.18** shows the calculated response at longitudinal strain gauge situated at middle of the slab. In this simulation, the values of the coefficients of creep compliance function were determined through creep tests (the method of calculation has been illustrated in **Chapter 7**) of samples cored from outside wheel path.

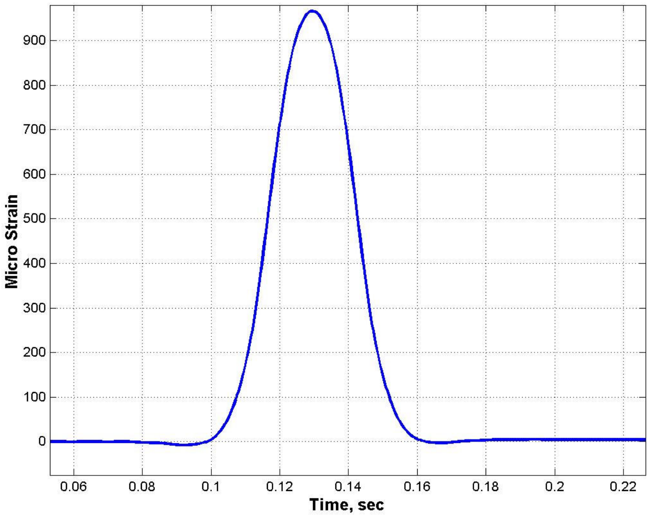

Figure 10.17: Calculated response at transverse strain gauge due to one pass

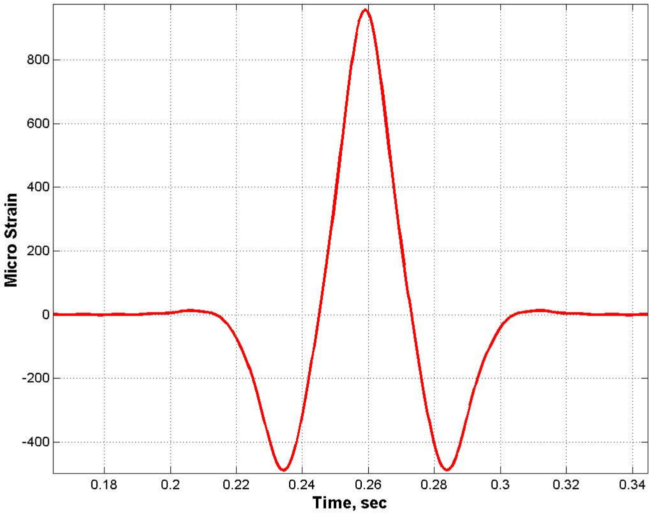

Figure 20.18: Calculated response at longitudinal strain gauge due to one pass

The **Figure 10.18** indicates the tension compression effects for longitudinal strain gauges, while **Figure 20.17** shows the tension only effect for transverse strain gauges. These are in accordance with the findings of the tests of HMA slabs. Note that the maximum strains are in the order of strains observed during tests.

10.11.6 Response During Rest Period

The response during rest period is easily obtained by retaining the integral under summation sign only and summing from $j = 0$ to $j = (p\text{-}1)T$:

$$\varepsilon(t) = A\sum_{m}\sum_{n}\sum_{j=0}^{p-1}\left(A_2 I_1(t) + A_3 I_2(t)\right), \text{ for } t > pT \qquad (10.23)$$

10.11.7 Permanent Strain

From **Eq. 10.20**, it can be seen that total response during loading can be expressed as the function of summation of two integrals, $I_\mathrm{I}(t)$ and $I_\mathrm{I}(t)$:

$$\begin{aligned} \varepsilon(t) &= A\sum_m \sum_n \left[I_I(t) + I_{II}(t)\right] \\ I_I(t) &= \sum_{j=0}^{p-2} \left(A_2 I_1(t) + A_3 I_2(t)\right) \\ I_{II}(t) &= A_1 P(t) + A_2 I_3(t) + A_3 I_4 \end{aligned} \tag{10.24}$$

Permanent or accumulated strain, $\varepsilon_p(t)$, is defined as the difference between strains observed at the end of two successive cycles, i.e., $\varepsilon_p(t) = \varepsilon(t+T) - \varepsilon(t)$. We have two parts of the total strain given in two integral formulations, $I_I(t)$ and $I_{II}(t)$, which are functions of time and model parameters. If any of these two integrals is periodic, that is $I(t) = I(t+T)$, then it contributes to zero permanent strain. On the other hand, if any one of them has the property $I(t+T) \neq I(t)$, then it contributes to nonzero permanent strain to total strain. We investigate each of them in this context.

The integral $I_I(t)$ contains integrals $I_1(t)$ and $I_2(t)$ and the integral $I_{II}(t)$ contains integrals $I_3(t)$, $I_4(t)$ and $A_1P(t)$. Therefore periodicity of integrals in **Eq. 20.21** constitutes the periodicity of integrals $I_I(t)$ and $I_{II}(t)$. The general form of integrals $I_1(t)$ and $I_2(t)$ can be written using **Eq. 10.21** and **Eq. 10.22** as:

$$I(t) = (\sum_{j=0}^{p-2} C_j)\exp(Bt)$$

$$C_j = -\frac{1}{1+\left(\frac{Bb}{n\pi V}\right)^2}\frac{b}{n\pi V}\exp(-BjT)\left[\begin{array}{l} \exp(-BT)\left\{\begin{array}{l}\cos\frac{n\pi V}{b}((j+1)T-(p-1)T) \\ +\frac{Bb}{n\pi V}\sin\frac{n\pi V}{b}((j+1)T-(p-1)T)\end{array}\right\} \\ -\cos\frac{n\pi V}{b}(jT-(p-1)T) \\ -\frac{Bb}{n\pi V}\sin\frac{n\pi V}{b}(jT-(p-1)T) \end{array}\right]$$

(10.25)

Considering two time instances $(p\text{-}1)T \leq t < pT$ and $pT \leq t < (p+1)\mathrm{T}$, we get:

$$I(t+T) - I(t) = [(\sum_{j=0}^{p-1} C_j)\exp(BT) - \sum_{j=0}^{p-2} C_j]\exp(Bt) \neq 0 \qquad (10.26)$$

Eq. 10.26 implies $I_1(t)$ and $I_2(t)$ are non-periodic and therefore $I_{\mathrm{I}}(t)$ is non-periodic. The last two integrals in **Eq. 10.21** can be written (using **Eq. 10.22**) as:

$$I(t) = -\frac{1}{1+\left(\frac{Bb}{n\pi V}\right)^2}\frac{b}{n\pi V}\left[\begin{array}{l}\cos\frac{n\pi V}{b}(t-(p-1)T) \\ +\frac{Bb}{n\pi V}\sin\frac{n\pi V}{b}(t-(p-1)T) - \exp(B(t-(p-1)T)\end{array}\right] \qquad (10.27)$$

From **Eq. 10.27**, we have,

$$I(t+T) - I(t) = 0 \qquad (10.28)$$

Eq. 10.28 implies $I_3(t)$ and $I_4(t)$ are periodic. We also notice that $A_1P(t)$ is periodic since $P(t)$ is periodic. Therefore, $I_{\mathrm{II}}(t)$ is periodic. Therefore, the permanent strain is given by:

$$\varepsilon_p(t) = [(\sum_{j=0}^{p-1} C_j)\exp(BT) - \sum_{j=0}^{p-2} C_j]\exp(Bt) \tag{10.29}$$

10.11.8 Conclusions from Analytical Model

Several important points can be observed from the equations of strain:

1. The model can simulate the viscoelastic time dependent behavior of HMA under moving wheel load under test conditions, which was not possible under elastic assumptions of finite element model presented earlier in this chapter. The finite element model can be used to estimate response under initial conditions, while the analytical model presented in this section can adequately represent time dependent behavior of test slabs under MMLS3 loading. The analytical model can be used to estimate viscoelastic strains under loading conditions specifically for MMLS3 loading conditions.

2. The model can be used for estimating strain at any temperature by using appropriate creep compliance functions at that particular temperature.

3. The study of the strain equations can provide a close look at the situations during cyclic loading, such as: total strain is a superposition of two time functions, one is periodic ($I_{II}(t)$) with period same as loading period and other is non-periodic ($I_I(t)$).

Chapter 11

CONTRIBUTIONS TO KNOWLEDGE

MMLS3 is a very realistic APT tool with features such as the ability to simulate field conditions in the laboratory and the ability to be used for fatigue characterization of HMA in the laboratory. If such equipment is used properly following a specified protocol, very meaningful and realistic data can be obtained.

This study attempted to determine a specific loading and testing protocol that would allow to employ this powerful equipment in a proper and practical way. Significant contributions of this study to the existing knowledge of APT and fatigue characterization of HMA are as follows:

1. A practical test protocol for fatigue characterization of HMA in the laboratory has been developed using the one-third scale Model Mobile Load Simulator.

2. It has been shown in this study that an improved fatigue response relationship can be obtained with this equipment compared to that can be obtained using any other conventional fatigue tests equipment such as beam fatigue test equipment.

3. An insight into the fatigue behavior of HMA can be obtained through the use of this equipment, which allows the user to observe rutting and fatigue simultaneously in test pavement. This also allows the user to separately investigate the two phenomena in a test.

4. An analytical model of the MMLS3 scaled pavement section has been developed in this study where contributions of periodic and permanent strain to the total strain have been obtained. This model can be used for parametric study before conducting a full MMLS3 tests.

Chapter 12

CONCLUSIONS AND RECOMMENDATIONS

12.1 Conclusions

Based on the observations from several fatigue tests involving preparation of test pavement slabs, loading, testing and analysis of data, the following conclusions can be made:

1. Fabrication of an instrumented scaled model pavement is feasible in a reasonable amount of time (e.g., within two days). This model pavement can be used to simulate rutting and fatigue damage in pavements with the use of the MMLS3.

2. A finite element model of the MMLS3 scaled pavement showed a reasonable way to calculate elastic response under MMLS3 loading while considering hyperelastic behavior of the neoprene sheet. The finite element model presented in this paper successfully described the behavior of MMLS3 model pavement observed in the laboratory in terms of strain distribution under HMA layer and similarity to field conditions.

3. The MMLS3 can be used for the evaluation of HMA fatigue performance and related material characterization. It has been shown in **Chapter 10** that characteristic curves showing the relation between fatigue life and strain can be developed using this equipment.

4. The fatigue performance of HMA using MMLS3 is expected to be closer to actual field performance with less uncertainty related to shift factors. This has been demonstrated through comparison of the MMLS3 fatigue characteristic curve with the characteristic curve obtained from standard beam fatigue test methods,

such as Asphalt Institute method (**Chapter 10**). The comparison showed that the two methods predict approximately same failure load at lower strain levels, but at higher strain levels failure loads predicted by MMLS3 are higher than those predicted by AI method.

5. The Combined effect of fatigue and rutting on pavement life can be investigated with the MMLS3. The MMLS3 has been shown to be useful for investigating the inter-relationship between deformation due to rutting and fatigue (**Chapter 10**).

6. In terms of protocols, it is apparent that it is necessary to limit or reduce the influence of factors that affect fatigue performance, such as temperature variation and compaction effort. Furthermore, rest periods for different tests slabs should be as far as possible equal in time span.

12.2 Recommendations

Based on the results obtained from this study it can be concluded that the MMLS3 has a strong potential for becoming an effective laboratory tool for material characterization. As such, proper specimen preparation, loading and testing protocols should be followed for this equipment. Such protocols are being developed by researchers in the United States as well as in South Africa, among other places. Once these protocols are available, the MMLS3 should be considered a regular laboratory tool. It can be used to characterize rutting and fatigue behavior of HMA, particularly with respect to the effects of material, traffic and environmental factors.

BIBLIOGRAPHY

[1] Metcalf J. B. “Accelerated Pavement Testing, A Brief Review Directed Towards Asphalt Interest.” Journal of the Association of Asphalt Paving Technologists, 1998.

[2] Hugo F., Smit A. de F. and Warren P. “Report on APT Data Survey”. Transportation Research Board, Research Circular, Interim Report, Number E-C004, February 1999.

[3] Proceedings of the First International Conference on Accelerated Pavement Testing, Reno, Nevada, 1999.

[4] Groenendijk J, Miradi A., Molenaar A.A.A., Dohmen L.J.M., Maagdenberg A.M. and de Beer M. “Pavement Performance Modeling Using LINTRACK”. Proceedings of the Eighth International Conference on Asphalt Pavements, Seattle, Washington, August 10-14, 1997.

[5] Groenendijk J. PhD Dissertation. Technical University of Delft (TuDelft), Netherland, 1997.

[6] Molenaar A. A. A., Groenendjik J., Dommelen A. Van. “Development of Performance Models from APT.” Proceedings of the First International Conference on Accelerated Pavement Testing, Reno, Nevada, 1999.

[7] White T. D, Hua J. and Galal K. “Analysis of Accelerated Pavement Tests.” Proceedings of the First International Conference on Accelerated Pavement Testing, Reno, Nevada, 1999.

[8] Harvey J. T., Hoover T., Coetzee N. F., Nokes W. A. and Rust F. C. “CALTRANS Accelerated Pavement Test (CAL/APT) Program – Test Results: 1994-1997.” Journal of the Association of Asphalt Paving Technologists, 1998.

[9] Brock J. D., Collins R. and Lynn C. “Performance Related Testing With the Asphalt Pavement Analyzer.” Technical Paper T-137, PTI, Covington, GA.

[10] IPC Global, www.ipcglobal.com.au.

[11] Aschenbrener T., Terrel R. L., Zamora R. A. “Comparison of the Hamburg Wheel Tracking Device and the Environmental Conditioning System to Pavements of Known Stripping Performance”. Report Number CDOT-DTD-R-94-1. January 1994.

[12] “French Rutter Test procedure; Standard Test Method for French Rutter”. Report, Colorado Dept of Transportation, May 6, 1996.

[13] Van-de-Ven M., Andre de-Fortier Smit, K Jenkins and F Hugo. “Scaled Down APT Considerations for Viscoelastic Materials.” Journal of the Association of Asphalt Paving Technologists, 1998, Vol 67, pp 602-622.

[14] Kim S-M, Hugo F, Roesset J. M. and White T. D. “Dimensional Analysis of the Model Mobile Load Simulator Action on Pavement.” Research Report 2914-1F, Center for Transportation Research, Bureau of Engineering Research, The University of Texas at Austin, March 1995.

[15] Kim S-M, Hugo F, Roesset J. M. “Small-Scale Accelerated Pavement Testing.” ASCE Journal of Transportation Engineering, 1998, Vol 124, No. 2, pp 117-122.

[16] Dijk Van. W. “Practical Fatigue Characterization of Bituminous Mixes.” Journal of the Association of Asphalt Paving Technologists, 1975, Vol 44, pp 38-74.

[17] Rowe G. M. and Brown S. F. “Validation of Fatigue Performance of Asphalt Mixtures with Small Scale Wheel Tracking Experiments.” Journal of the Association of Asphalt Paving Technologists, 1997, Vol 66, pp 31-73.

[18] Hugo F. “Some Notes On Tests With The MMLS MK3 On Full-Scaled Pavements.” April 25, 2000.

[19] Hugo F., Smit A. de F. and Epps A. “A Case Study Of Model APT In The Field.” Proceedings of the First International Conference on Accelerated Pavement Testing, Reno, Nevada, 1999.

[20] Hugo F. and Poolman P. “A Critical Analysis of WesTrack MMLS3 and Truck Rut Data.” Appendix A in Report 2134-1 of Project 2134 by Epps A. L., Ahmed T., Little D. C. and Hugo F. for Texas Department of Transportation.

[21] Hugo F. and Poolman P. “A Critical Review of the Quantitative Analysis of MMLS3 and Truck Rutting Performance At WesTrack.” Appendix B in Report 2134-1 of Project 2134 by Epps A. L., Ahmed T., Little D. C. and Hugo F. for Texas Department of Transportation.

[22] Epps A. L., Walubita L. F., Hugo F. and Bangera N. U. “Comparing Pavement Response and Rutting Performance for Full Scale and One Third Scale Accelerated Pavement Testing.” Proceedings of Transportation Research Board Meeting, Washington DC, January 2001.

[23] Epps A. M., Ahmed T. and Little D. C. and Hugo F. “Performance Prediction With the MMLS3 at WesTrack”. Report No. 2134-1, Texas A&M University, March, 2001.

[24] Smit A. dF., Walubita L., Jenkins K. and Hugo F. “The Model Mobile Load Simulator As a Tool for Eavluating Asphalt Performance Under Wet Condition.” Proceeding of the Ninth International Conference on Asphalt Pavements, Copenhagen, August, 2002.

[25] Walubita, L.F., Hugo, F., Epps Martin, A. “Indirect Tensile Fatigue Performance of Asphalt After MMLS Trafficking Under Different Environmental Conditions.” Journal of the South African Institution of Civil Engineering, Johannesburg, South Africa, 2002, Vol. 44, Number 3.

[26] Lee S. J. and Kim Y. R. “Development of Fatigue Cracking Test Protocol and Life Prediction Methodology Using the Third Scale Model Mobile Load Simulator.” Proceedings of the Fifth International RILEM Conference, Limoges, France, May, 2004.

[27] Timoshenko S. P. and Goodier J. N. Theory of Elasticity. Text Book, Third Edition, 1970, McGraw-Hill International Edition.

[28] Foamed Bitumen Mix Design Procedure Using The Wirtgen WLB 10. Reference manual published by Wirtgen America Inc. 6030 Dana Way, Nashville, TN 37013, USA.

[29] Workzone Overhead Workshop Heater. W.B. Marvin Manufacturing Company, 211 Glenn Avenue, Urbana, Ohio, 43078.

[30] Industrial Food Grade Silicon Lubricant. CRC Industrial Inc. Warminster, PA, 18974.

[31] Bhattacharjee, S. and Mallick R. B. “An Alternative Approach for the Determination of Bulk Specific Gravity and Permeability of Hot Mix Asphalt (HMA).” International Journal of Pavement Engineering, Vol 3, No 3, September 2002.

[32] Hunag, Y.H. Pavement Analysis and Design. Text Book, Second Edition, 2004, Prentice Hall, Englewood Cliffs, NJ, 07632.

[33] McMillan C. and Palsat D. “A Review of Alberta Transportation Mix Type Selection Criteria.” Proceedings of Canadian Technical Asphalt Association, 2002.

[34] ABAQUS Standard Software User’s Manual, ABAQUS Inc, Summit Office Park, West Building, 300 Centerville Road, Suite 209W, Warwick, RI 02886-0201.